Check for updates

Received: 9 October 2024 | Revised: 10 December 2024 | Accepted: 26 December 2024

DOI: 10.1002/mrm.30424

GUIDELINES

Magnetic Resonance in Medicine

Considerations and recommendations from the ISMRM Diffusion Study Group for preclinical diffusion MRI: Part 3—Ex vivo imaging: Data processing, comparisons with microscopy, and tractography

Kurt G. Schilling[1,2] | Amy F. D. Howard[3,4] | Francesco Grussu[5,6] | Andrada Ianus[7,8] | Brian Hansen[9] | Rachel L. C. Barrett[10,11] | Manisha Aggarwal[12] | Stijn Michielse[13] | Fatima Nasrallah[14] | Warda Syeda[15] | Nian Wang[16,17] | Jelle Veraart[18] | Alard Roebroeck[19] | Andrew F. Bagdasarian[20,21] | Cornelius Eichner[22] | Farshid Sepehrband[23] | Jan Zimmermann[24] | Lucas Soustelle[25] | Christien Bowman[26,27] | Benjamin C. Tendler[28] | Andreea Hertanu[29] | Ben Jeurissen[30,31] | Marleen Verhoye[26,27] | Lucio Frydman[32] | Yohan van de Looij[33] | David Hike[20,21] | Jeff F. Dunn[34,35,36] | Karla Miller[4] | Bennett A. Landman[37] | Noam Shemesh[8] | Adam Anderson[2,38] | Emilie McKinnon[39] | Shawna Farquharson[40] | Flavio Dell'Acqua[41] | Carlo Pierpaoli[42] | Ivana Drobnjak[43] | Alexander Leemans[44] | Kevin D. Harkins[1,2,45] | Maxime Descoteaux[46,47] | Duan Xu[48] | Hao Huang[49,50] | Mathieu D. Santin[51,52] | Samuel C. Grant[20,21] | Andre Obenaus[53,54] | Gene S. Kim[55] | Dan Wu[56] | Denis Le Bihan[57,58] | Stephen J. Blackband[59,60,61] | Luisa Ciobanu[62] | Els Fieremans[63] | Ruiliang Bai[64,65] | Trygve B. Leergaard[66] | Jiangyang Zhang[67] | Tim B. Dyrby[68,69] | G. Allan Johnson[70,71] | Julien Cohen-Adad[72,73,74] | Matthew D. Budde[75,76] | Ileana O. Jelescu[29,77]

Correspondence
Kurt G. Schilling, Radiology and Radiological Sciences, Vanderbilt University Medical Center, Nashville, TN, USA.
Email: kurt.g.schilling.1@vumc.org

Funding information
Government of Catalonia, Grant/Award Number: 2020 BP 00117; National Institute on Drug Abuse, Grant/Award Number: P30DA048742; National

Abstract

Preclinical diffusion MRI (dMRI) has proven value in methods development and validation, characterizing the biological basis of diffusion phenomena, and comparative anatomy. While dMRI enables in vivo non-invasive characterization of tissue, ex vivo dMRI is increasingly being used to probe tissue microstructure and brain connectivity. Ex vivo dMRI has several experimental advantages that facilitate high spatial resolution and high SNR images, cutting-edge diffusion contrasts, and direct comparison with histological data as a methodological

Kurt G. Schilling and Ileana O. Jelescu contributed equally to this work.

For affiliations refer to page 16

This is an open access article under the terms of the Creative Commons Attribution License, which permits use, distribution and reproduction in any medium, provided the original work is properly cited.
© 2025 The Author(s). *Magnetic Resonance in Medicine* published by Wiley Periodicals LLC on behalf of International Society for Magnetic Resonance in Medicine.

Institute of Biomedical Imaging and Bioengineering, Grant/Award Numbers: R01EB031765, R56EB031765; National Institutes of Health, Grant/Award Numbers: K01EB032898, R01AG057991, R01CA160620, R01EB017230, R01EB019980, R01EB031954, R01NS109090, R01NS125020; NSERC; Research Center of Excellence of the University of Antwerp; Research Foundation Flanders, Grant/Award Numbers: FWO, 12M3119N; la Caixa, Grant/Award Number: LCF/BQ/PR22/11920010; Canada Foundation for Innovation, Grant/Award Numbers: 32454, 34824; CIHR, Grant/Award Number: FDN-143263; Canadian Institute of Health Research, Grant/Award Number: CIHRFDN-143263; European Research Council, Grant/Award Number: 101044180; Swiss National Science Foundation; Quebec BioImaging Network, Grant/Award Number: 5886,35450; Natural Sciences and Engineering Research Council of Canada, Grant/Award Number: RGPIN-2019-07244; Fonds de Recherche du Québec - Santé, Grant/Award Number: 322736; Wellcome Trust, Grant/Award Numbers: 202788/Z/16/A, 203139/A/16/Z, 203139/Z/16/Z; Eccellenza Fellowship, Grant/Award Number: PCEFP2_194260

validation. However, there are a number of considerations that must be made when performing ex vivo experiments. The steps from tissue preparation, image acquisition and processing, and interpretation of results are complex, with many decisions that not only differ dramatically from in vivo imaging of small animals, but ultimately affect what questions can be answered using the data. This work concludes a three-part series of recommendations and considerations for preclinical dMRI. Herein, we describe best practices for dMRI of ex vivo tissue, with a focus on image pre-processing, data processing, and comparisons with microscopy. In each section, we attempt to provide guidelines and recommendations but also highlight areas for which no guidelines exist (and why), and where future work should lie. We end by providing guidelines on code sharing and data sharing and point toward open-source software and databases specific to small animal and ex vivo imaging.

KEYWORDS

acquisition, best practices, diffusion MRI, diffusion tensor, ex vivo, microstructure, open science, preclinical, processing, tractography

1 | INTRODUCTION

The use of animal models and ex vivo tissue is essential to the field of diffusion MRI. In this work, we define small animal imaging as imaging performed on a living experimental animal, whereas ex vivo we define as covering any fresh excised tissue, perfused living tissue, or fixed tissue. Small-animal research is highly valuable for investigating the biology, etiology, progression, and treatment of disease; for the field of dMRI specifically, preclinical imaging is essential for methodological development and validation, characterizing the biological basis of diffusion phenomena, and comparative anatomy. While dMRI enables non-invasive characterization of tissue in vivo, ex vivo acquisitions are increasingly being used to probe tissue properties and brain connectivity. Diffusion MRI of ex vivo tissue has several experimental advantages, including longer scanning times and absence of motion. Together, these make it possible to acquire data with significantly higher SNR, higher spatial resolution, and with sophisticated diffusion contrasts which may enable better characterization of tissue microstructure and structural connectivity. Another advantage afforded by ex vivo dMRI is the ability to compare diffusion data to histological data, bridging the gap between in vivo and histology for methodological validation. Because of these advantages, there have been an increasing number of dMRI studies on ex vivo tissue samples.

However, there are a number of considerations that must be made when performing ex vivo experiments. The steps from tissue preparation, image acquisition and processing, and interpretation of results are complex, with many decisions that not only differ dramatically from in vivo imaging of small animals, but ultimately affect what questions can be answered using the data. This work completes a three-part series of recommendations and considerations for preclinical diffusion MRI. Part 1 (30429) focuses on small animal diffusion MRI,[1] giving guidance for in vivo acquisition protocols and data processing. Part 2 (30435) presents best practices for dMRI acquisitions in ex vivo tissue covering hardware selection, fixation and sample preparation, MR scanning, and tissue storage. In this manuscript, Part 3, we discuss and give recommendations for everything that follows ex vivo acquisition: image

15222594, 0, Downloaded from https://onlinelibrary.wiley.com/doi/10.1002/mrm.30424 by Ecole Polytech De Montreal, Wiley Online Library on [14/03/2025]. See the Terms and Conditions (https://onlinelibrary.wiley.com/terms-and-conditions) on Wiley Online Library for rules of use; OA articles are governed by the applicable Creative Commons License

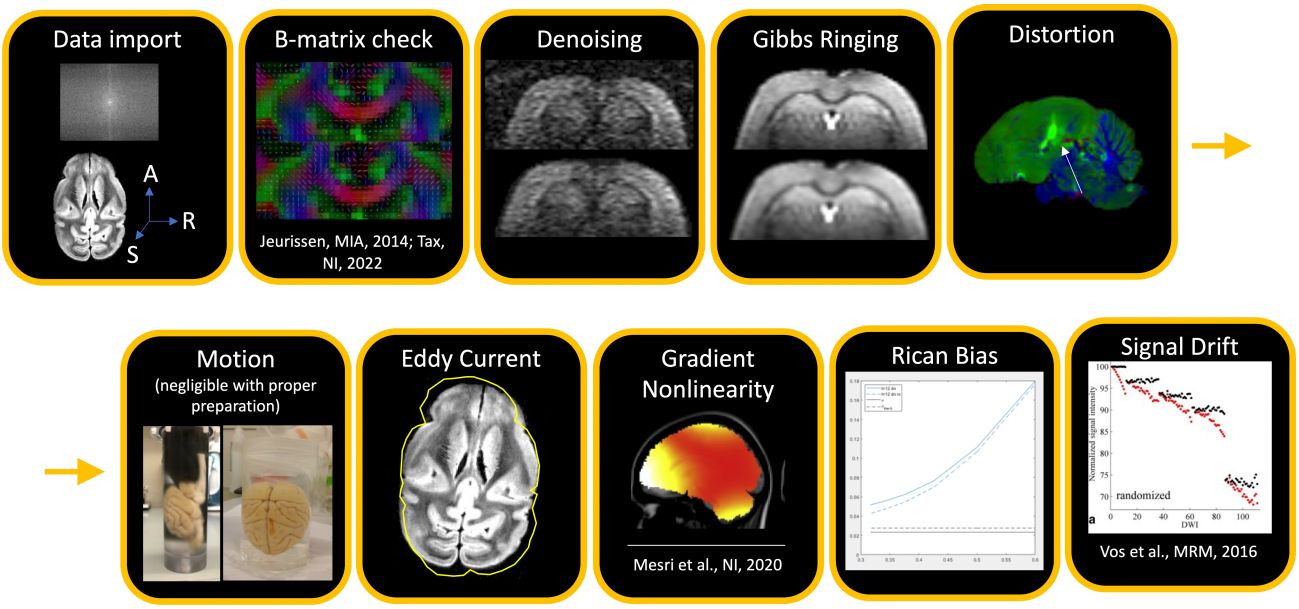


FIGURE 1 There are many artifacts that must be corrected for in preprocessing. These are not necessarily presented in order, and correction may not be necessary in all cases. Nevertheless, the most common order for pre-processing steps (after data important and quality check) is: (i) thermal noise reduction (referred to as denoising), (ii) Gibbs ringing correction, (iii) susceptibility distortion + motion + eddy current corrections (+ gradient non-linearity, if applicable), (iv) Rician bias correction and (v) signal drift correction. Figures kindly provided by Ileana Jelescu, Kurt Schilling, or reproduced from.[2,3]

pre-processing, diffusion quantification and/or model fitting, methodologies for comparisons with histology, and ex vivo fiber tractography. Finally, we give perspectives on the field, describing sharing of code and data, and goals that we wish to achieve. In each section, we attempt to provide recommendations and considerations, also highlight areas for which no recommendations exist (and why), and where future work should lie. An overarching goal herein is to enhance the rigor and reproducibility of ex vivo dMRI acquisitions and analyses and, thereby, advance biomedical knowledge.

This work does not serve as a "consensus" on any specific topic, but rather as a snapshot of "best practices" or "recommendations" from the preclinical dMRI community as represented by the authors. We envision this work to be useful to imaging centers using small animal scanners for research, sites that may not have personnel with expert knowledge in diffusion, pharmaceutical or industry employees, or new trainees in the field of dMRI. The resources provided herein may act as a starting point when reading the literature and understanding the decisions and processes for studying model systems with dMRI.

2 | DATA PRE-PROCESSING

In this paper we refer to *pre-processing* as steps that come before any diffusion fitting (tensors, biophysical models, etc.). Pre-processing thus includes data conversion (e.g., DICOM to NIfTI), noise reduction, artifact correction/mitigation, or any step that aims at improving data quality. Processing refers to diffusion data fitting and normalization to standard space. See Figure 1 for possible preprocessing steps.

Ex vivo diffusion MRI suffers from many of the same artifacts that in vivo imaging of both small animals and humans are susceptible to. These include thermal noise, Gibbs ringing, signal drift, eddy current and susceptibility distortions, and sample motion. Below, we detail the steps associated with a typical pre-processing pipeline, stressing in particular what may differentiate implementations of ex vivo imaging from in vivo, and how available tools can/should be modified accordingly.

While most pipelines are designed for, and most heavily used in the brain, similar artifacts occur in all dMRI images. Our recommendations are generically applicable for all organs scanned ex vivo, although most details below are specific to brain imaging.

Any pipeline, regardless of sample, begins with data importation and reconstruction. While preclinical vendor software may output data in vendor-specific formats, common diffusion preprocessing software is most easily compatible with NIfTI or DICOM data, which stores not only the image matrix but also header information that includes information such as spatial resolution, sample orientation, and often acquisition parameters. With diffusion

15222594, 0, Downloaded from https://onlinelibrary.wiley.com/doi/10.1002/mrm.30424 by Ecole Polytech De Montreal, Wiley Online Library on [14/03/2025]. See the Terms and Conditions (https://onlinelibrary.wiley.com/terms-and-conditions) on Wiley Online Library for rules of use; OA articles are governed by the applicable Creative Commons License

data, the diffusion weighting and diffusion directions are often stored as accompanying *b*-value and *b*-vector text files. The orientation of the images with respect to the applied diffusion directions is important, particularly for tractography, and should be quality checked carefully.[4,5] This is particularly important ex vivo where samples may be oriented differently to the living model. Consequently, header information which describes the orientation of the images (i.e., the Left–Right, Inferior–Superior, Anterior–Posterior labels) may need correcting and it is often commonplace to put some identifiable object (such as a fluid-filled capsule) or even a small physical cut in one hemisphere to ensure the hemispheres are correctly labeled. Tools for importation, reconstruction, conversion, and b-table quality control are given in Section 5.1.1.

A prerequisite for many preprocessing steps is generating a brain mask. The mask is often used to save computation time or optimize areas on the image to focus corrections on. In general, brain mask generation can be challenging for small animal models because most digital "brain extraction" tools are optimized for and validated on the human brain. This can be more straightforward for ex vivo images, particularly if the sample was skull-extracted and immersed in perfluorocarbon fluids (e.g., fomblin) for imaging. One species agnostic approach for digitally extracting the brain from the image background that performs well on ex vivo images is to threshold the non-diffusion weighted image based on signal intensity, perform iterative dilation/erosion, and remove non-connected components.[6] When tissue is scanned within the skull, alternatively, species-specific strategies may be adopted.[7,8] One approach is to register all brains to a common space (template or atlas) where a brain mask is available or can be derived. The brain mask can then be registered back to native space, and optionally further adapted at the subject level.[8]

Next, denoising aims to reduce thermal noise in diffusion-weighted images. Most denoising approaches and associated requirements are un-changed for ex vivo diffusion MRI. For example, a common approach based on principal component analysis (PCA)[9] and automated identification of signal and noise-carrying components (MP-PCA,[10] NORDIC[11]) has proven useful in dMRI and is therefore recommended. The requirements here are that the noise level is constant across all diffusion images and that the number of diffusion images is large, where we suggest the use of >30 images. Other methods, for example total variation minimization[12] or non-local means denoising[12,13] are also applicable to ex vivo images. Several algorithms and packages are also provided in Section 5.1.1. It is worth noting that most denoising methods assume Gaussian noise, whereas MR signal in magnitude images follows a Rician or non-chi-squared distribution. Consequently, denoising should be ideally performed using complex or real-valued images to avoid enhancement of the rectified noise floor that may affect downstream modeling (see[14] for further discussion). We note that the MP-PCA algorithm can output a map of the noise level (σ) at each voxel, which can be used to calculate SNR maps for each diffusion-weighted image (by dividing the signal S by σ). A rule of thumb is that the SNR should be at least 2–5 for the highest *b*-value (note that it is also direction-dependent).

The next suggested step is Gibbs ringing correction, which is an artifact that appears as signal oscillations next to high contrast tissue interfaces and can interfere with model fitting for voxels near tissue edges, for example, in the corpus callosum[15] or cortex, which are close to CSF. Gibbs ringing correction, while not dramatically affecting tractography, is important for microstructure modeling. Correction techniques include the methods described in[16] when a full Fourier acquisition is acquired and that of[17] when partial-Fourier acquisition is used (both for 2D multi-slice imaging). These methods have recently been extended to 3D,[18] which is appropriate for the 3D acquisitions common in ex vivo imaging.

Next, susceptibility distortions, eddy currents, and sample motion need to be corrected. While susceptibility distortion in ex vivo scans can be mitigated through a multi-shot (segmented) acquisition, and motion should be minimal (with proper sample preparation), we still recommend correction for these potential artifacts. Pipelines and algorithms, such as those implemented within FSL (using the topup and eddy tools) or within TORTOISE (using the DR BUDDI tool) utilize a reverse phase encode scan to estimate the distortion field and may use this field while correcting all three artifacts simultaneously. Regardless of software, care should be taken when using these pipelines with default parameters or configurations. For example, the knot-spacing or warp-field resolution for distortion/warping fields are typically set for human data acquired at ~2–2.5 mm isotropic resolution and should be scaled to match the possibly higher resolution ex vivo data under investigation. Additionally, practical compromises may need to be made (for example when choosing the number of iterations to run, or downsampling factors within the pipeline) for time considerations, particularly for ultra-high resolution datasets acquired with many diffusion-weightings.

Rician bias correction corrects the diffusion signal decay by subtracting the non-zero Rician floor that is present in magnitude data. Typical methods will assume the Gaussian noise standard deviation to be known, for example, as previously estimated using MP-PCA on low *b*-value data. For software and methods, see[19,20] and

15222594, 0, Downloaded from https://onlinelibrary.wiley.com/doi/10.1002/mrm.30424 by Ecole Polytech De Montreal, Wiley Online Library on [14/03/2025]. See the Terms and Conditions (https://onlinelibrary.wiley.com/terms-and-conditions) on Wiley Online Library for rules of use; OA articles are governed by the applicable Creative Commons License

Section 5.1.1. Alternatively, Rician noise models can be directly incorporated into the fitting procedure.

Finally, temporal instability on the scanner can cause signal drift, especially for diffusion sequences where strong gradients are employed for extended periods of time, even more so on preclinical scanners and especially for multi-day ex vivo experiments. This decrease in signal intensity over time can cause mis-estimates of derived parameters and also affect tractography.[3] Strategies to alleviate this effect include randomizing diffusion gradient directions and *b*-values, or better, explicitly designing direction sets to avoid consecutive directions with particularly heavy load on any one gradient axis. The presence of signal drift can be examined and corrected by collecting multiple $b=0$ images throughout the scan to determine correction factors (typically linear or quadratic) to minimize this effect. Although this is not commonly done in the literature, we advocate for its use, and methodology and code to do so is described in[3] and in Section 5.1.1.

3 | DATA PROCESSING

Data processing includes fitting, normalization to a standard space, and tractography analysis. Diffusion analysis differences between in vivo and ex vivo are along the same lines as differences outlined for setting up the acquisition protocol (see Part 2), that is, all changes are a direct result of potential differences/alterations in compartment sizes, diffusivities and relaxivities that are affected by chemical fixation and temperature.

3.1 | DTI/DKI

To ensure that the assumptions underpinning DTI and diffusion kurtosis imaging (DKI) are valid, the *b*-values need to be set such that $b\times D\sim 1$ (DTI limit), and $b\times D\sim 2$–3 (DKI limit)[21] (where D is the diffusivity). This means that the maximum recommended *b*-values depend on the diffusivity and thus on the temperature at which the data were acquired. As described in Part 1,[1] these guidelines result in a commonly used $b\simeq 1000\,\mathrm{s/mm^2}$ for DTI and highest *b*-value of $b\simeq 2000$–$2500\,\mathrm{s/mm^2}$ for DKI in vivo. As described in Part 2, ex vivo *b*-values should be increased by a factor of 2–5× depending on the drop in diffusivity. This means ex vivo DTI estimation can/should be performed based on *b*-values of $b\simeq 2000$–$5000\,\mathrm{s/mm^2}$, and the kurtosis tensor estimated from at least two shells with the highest *b*-value of $b\simeq 4000$–$10\,000\,\mathrm{s/mm^2}$.

There is clearly a wide range of possibly "optimal" *b*-values (we note that the lower end of these ranges are more typical in the literature). However, ex vivo also comes with the advantage that cursory scans should be used to investigate signal attenuation at different *b*-values for a given fixation and sample preparation procedure. The suitable *b*-value range for DTI and DKI analysis of a given ex vivo sample should be confirmed by examining the signal decay as a function of *b*-value to confirm the range of linear behavior (DTI regime: $\ln(S)\sim -bD$) and measurable curvature for kurtosis quantification ($\ln(S)\sim -bD+\frac{1}{6}\times(bD)^2K$). It should be noted that DKI estimation is affected by the choice of *b*-values and post-processing (fitting procedures).

3.2 | Biophysical modeling

For biophysical models, recommended *b*-values for optimal accuracy and precision of parameter estimation should also be adjusted ex vivo. Again, *b*-values should often be 2–5× the in vivo counterparts to account for the equivalent drop in water diffusivity. Similarly, diffusion times may need to be adjusted to account for this slower water diffusion ex vivo. See Part 2 for further discussion of ex vivo acquisitions.

At the parameter estimation level, priors on diffusivities should be adapted to match ex vivo values, as well as potential admitted bounds on parameter values and algorithm initialization values. A typical example of this is an 'ex vivo flag' in the original implementation and source code of the NODDI model[22] which changed the assumed fixed diffusivity from 1.7E-6 to 0.6E-6 $\mathrm{mm^2/s}$. This assumes the ex vivo diffusivity to be ∼1/3 of its in vivo value. However, as noted elsewhere, ex vivo diffusivities are highly sample (fixation) and temperature dependent, making "universal" assumptions about ex vivo diffusivities often unreliable. Importantly, biophysical models may need to be adapted dramatically by the exclusion of compartments related to CSF, and inclusion of additional compartments, such as the "dot" compartment (trapped water with extremely low diffusion coefficient, see previous Section 2.2 "Ex vivo: Translation and validation considerations"),[23] for which in vivo evidence is limited to the cerebellum[24,25] and ex vivo more widespread to the cerebrum,[26,27] spinal cord,[28] and optic nerve.[29] As it can be difficult to know a priori whether an additional dot compartment is justified ex vivo, and because it can be challenging to disentangle it from the Rician noise floor, best practice can include fitting multiple models (with and without the dot) and determining model selection via, for example, estimate plausibility (parameters within biological ranges), precision, and the corrected Akaike or Bayesian information criterion. Example DTI, DKI, and biophysical model parameters maps for ex vivo mouse brains are shown in Figure 2.

15222594, 0, Downloaded from https://onlinelibrary.wiley.com/doi/10.1002/mrm.30424 by Ecole Polytech De Montreal, Wiley Online Library on [14/03/2025]. See the Terms and Conditions (https://onlinelibrary.wiley.com/terms-and-conditions) on Wiley Online Library for rules of use; OA articles are governed by the applicable Creative Commons License

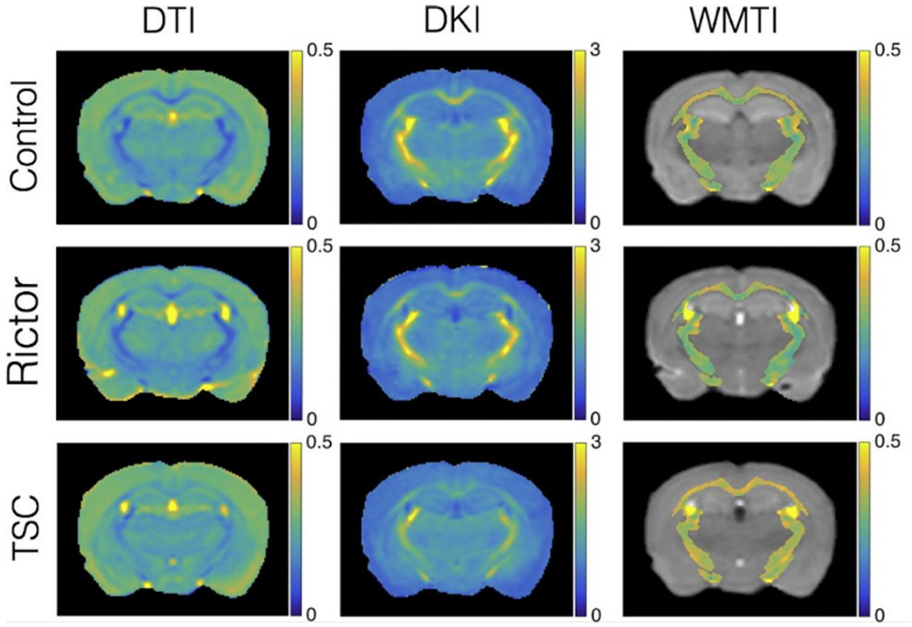


FIGURE 2 Ex vivo maps from DTI, DKI, and a biophysical model (white matter tract imaging; WMTI).[30] Parameter maps show radial diffusivity (DTI), radial kurtosis (DKI), and radial extra-axonal diffusivity (WMTI) for control mice and two hypomyelinated mouse models (Rictor and TSC). Ex vivo imaging was performed on a 15.2T Bruker Biospec scanner at 150 μm isotropic resolution using a 3D diffusion-weighted fast spin-echo and *b*-values of 3000 and 6000 s/mm^2. Figure reproduced from Ref. 31.

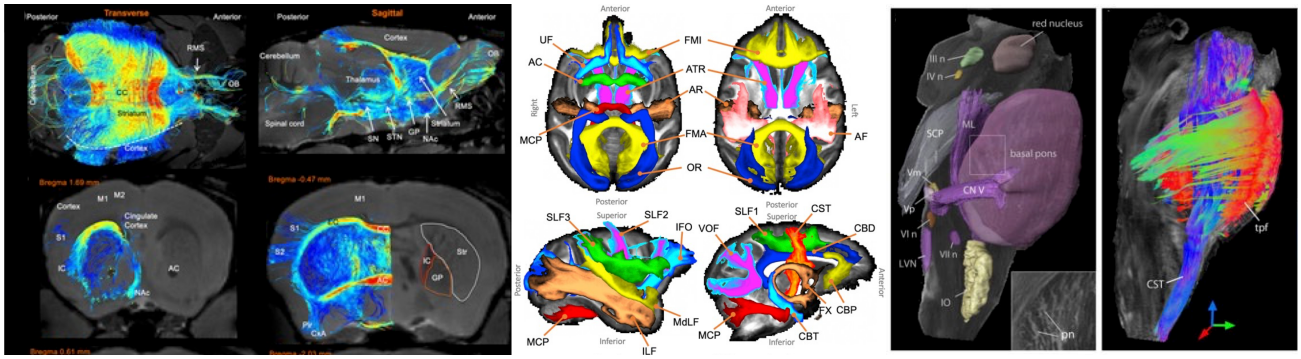


FIGURE 3 Ex vivo tractography on mouse (left),[32] macaque (middle), and human brains (right). In the mouse, high resolution tractography was used to identify region-to-region differences in connectivity in models of Huntington's disease; here, tractography is able to delineate Striatal connectivity. In the Macaque brain, standardized protocols were developed to enable robust and automated segmentation of 42 white matter pathways.[33] In the human brain, diffusion data at high spatial resolution showed feasibility of reconstructing brainstem nuclei and white matter of the brainstem.[34]

3.3 | Tractography

The application and use of fiber tractography as a tool to study the fiber pathways and wiring diagram of the brain remain largely the same for ex vivo (Figure 3) as for in vivo small animal and human dMRI, as fixation preserves the structure of axon bundles. In general, a measure of fiber orientation is estimated for each voxel, which is used to create continuous space curves (i.e., streamlines) which are thought of as representations of groups of axons traveling throughout the tissue. For these reasons, the fundamentals of tractography (deterministic and probabilistic algorithms) also remain the same, and guidelines follow that of human data.

For acquisition, we recommend acquiring data with isotropic resolution, as anisotropic voxel size can introduce bias in estimates of fractional anisotropy and hinder the ability of algorithms to deal with branching/bending pathways.[35] Higher angular resolution and strong diffusion weightings are likely to benefit tractography, particularly for small pathways, pathways near ventricles or gray matter boundaries, or pathways with high curvature. For most reconstruction techniques, we recommend acquiring greater than 30 diffusion-weighted directions (and commonly 60–100+, especially with little-to-no scan time limits). Example acquisitions with subsequent validation that have demonstrated reliable tractography results include the ex vivo mouse (0.1-mm resolution, 60 directions, $b = 5000$[36]), ex vivo ferret (0.24-mm resolution, 200 directions, $b = 4000$[37]), ex vivo squirrel monkey (0.3-mm resolution, 30–100 directions, $b = 1000$–$12'000$[37–39]), ex vivo macaque (0.25-mm resolution, $b = 4900$, 114

15222594, 0, Downloaded from https://onlinelibrary.wiley.com/doi/10.1002/mrm.30424 by Ecole Polytech De Montreal, Wiley Online Library on [14/03/2025]. See the Terms and Conditions (https://onlinelibrary.wiley.com/terms-and-conditions) on Wiley Online Library for rules of use; OA articles are governed by the applicable Creative Commons License

directions[40]; 0.5-mm resolution, $b = 1477–8040$, 180 directions[41,42]), and ex vivo pig (0.5-mm resolution, $b = 4000$, 61 directions[43]) — all b-values given in units of s/mm^2.

The next step in the tractography process is estimating a fiber orientation for every voxel in the image. For ex vivo imaging, very little changes occur for this step, as most reconstruction techniques, including DTI,[44] spherical deconvolution,[45] ball & sticks models,[46] and q-ball imaging,[47] will result in a field of orientation estimates that can be used for tractography. As above, some fiber reconstruction methods may be adapted for ex vivo data through the inclusion of a dot-compartment to avoid estimation of spurious fiber orientations due to overfitting.[48] One important point to emphasize ex vivo is that several deconvolution methods may estimate a response kernel (the diffusion signal that results from a single fiber population) including an isotropic free water or CSF component,[49] or may estimate a kernel for each tissue type: white matter, gray matter, CSF.[50,51] Because ex vivo tissue may not have CSF, or any free water if immersed in fomblin, care should be taken when using these algorithms to ensure they do not bias the true tissue components.

The tractography process itself is also largely unchanged ex vivo. As described in Part 1,[1] it is still important to consider, and adapt, parameters that can be tuned. For example, the step-size (the size of steps when propagating streamlines), curvature threshold (which stops streamlines if curvature is too high), or length thresholds (only allowing streamlines that are between a minimum and maximum total length). Adaptations should be considered based on acquired resolution, expected curvature of pathways under investigation, and length/size of the brain. For these reasons, most software packages for tractography (MRTrix3, DSI Studio, DIPY, FSL, ExploreDTI) are able to easily be used for ex vivo dMRI with few modifications.

Applications of tractography include bundle segmentation, the process of virtually selecting and dissecting pathways to study, and connectome analysis, assessing streamlines throughout the full brain to determine network properties, for example, using graph-theoretic measures. Recommendations for these are identical to that for in vivo imaging (see Part 1[1]), where the primary challenges associated with small animals are the lack of automated bundle dissection tools in different species, and a lack of (or challenges in identifying) cortical parcellation schemes to use for connectome analysis.

Additional tractography applications involve the ability to study species beyond those conventionally used as scientific models. A few select examples include multiple primate brains for comparative anatomy and insight into brain evolution,[52] studying auditory pathways in studies of dolphin brains,[53] toxic exposure effects on connectivity (and parallels to temporal lobe epilepsy) in sea lions,[54] or studying the extinct Tasmanian tiger brain[55] (preserved in formalin since 1905!) which have been extinct since 1936.

Finally, ex vivo imaging enables tractography in structures that may be challenging in vivo due to small size or motion. Examples include gray matter and intricate brainstem pathways in the human brain,[56–60] or detailed mapping of the ascending/descending white matter, intra-cortical connections, and collateral fibers of the ex vivo spinal cord.[61–63] Outside the central nervous system, tractography has proven useful for characterizing normal and abnormal myofiber architecture and depicting sub-divisions of the ex vivo heart,[64–66] or visualizing the course and structural abnormalities of ex vivo peripheral nerves,[67–71] or tracing renal structures at high resolution in the ex vivo kidney.[72] While we do attempt to provide specific guidelines for these structures, we recommend strongly considering the goal of the tractography process in these locations (determining trajectory or orientation of tissue? Clustering structures? Measuring spatial extent of structures?) and how choices in the tractography process, including start/stop criteria, length and curvature thresholds, and streamline propagation methods may influence the ability to perform the desired tractography process.

3.4 | Normalization/registration

It is common to use registration either to import atlas-based segmentation of brain regions (for region of interest [ROI] analysis or to use as tractography masks) or to bring individual maps into a common space for voxel-based comparisons. For this registration/normalization step, typical tools used in human data also work well for animal data, both in vivo and ex vivo, but often require some customization. For non-linear registration for instance, default physical dimensions of warp and smoothing kernels should be scaled to those of small-animal brains. Due to relaxation time and resolution differences in vivo versus postmortem, contrast between tissues may vary, and it can be challenging to non-linearly register ex vivo images to existing in vivo atlases (especially if the default cost-function is sum-squared-differences). In this case, it may be necessary to change the cost function (to mutual information, for example) or register to an explicit ex vivo atlas. Common MRI atlases, including brain segmentation, for a variety of species are provided in Section 5.1.2.

15222594, 0, Downloaded from https://onlinelibrary.wiley.com/doi/10.1002/mrm.30424 by Ecole Polytech De Montreal, Wiley Online Library on [14/03/2025]. See the Terms and Conditions (https://onlinelibrary.wiley.com/terms-and-conditions) on Wiley Online Library for rules of use; OA articles are governed by the applicable Creative Commons License

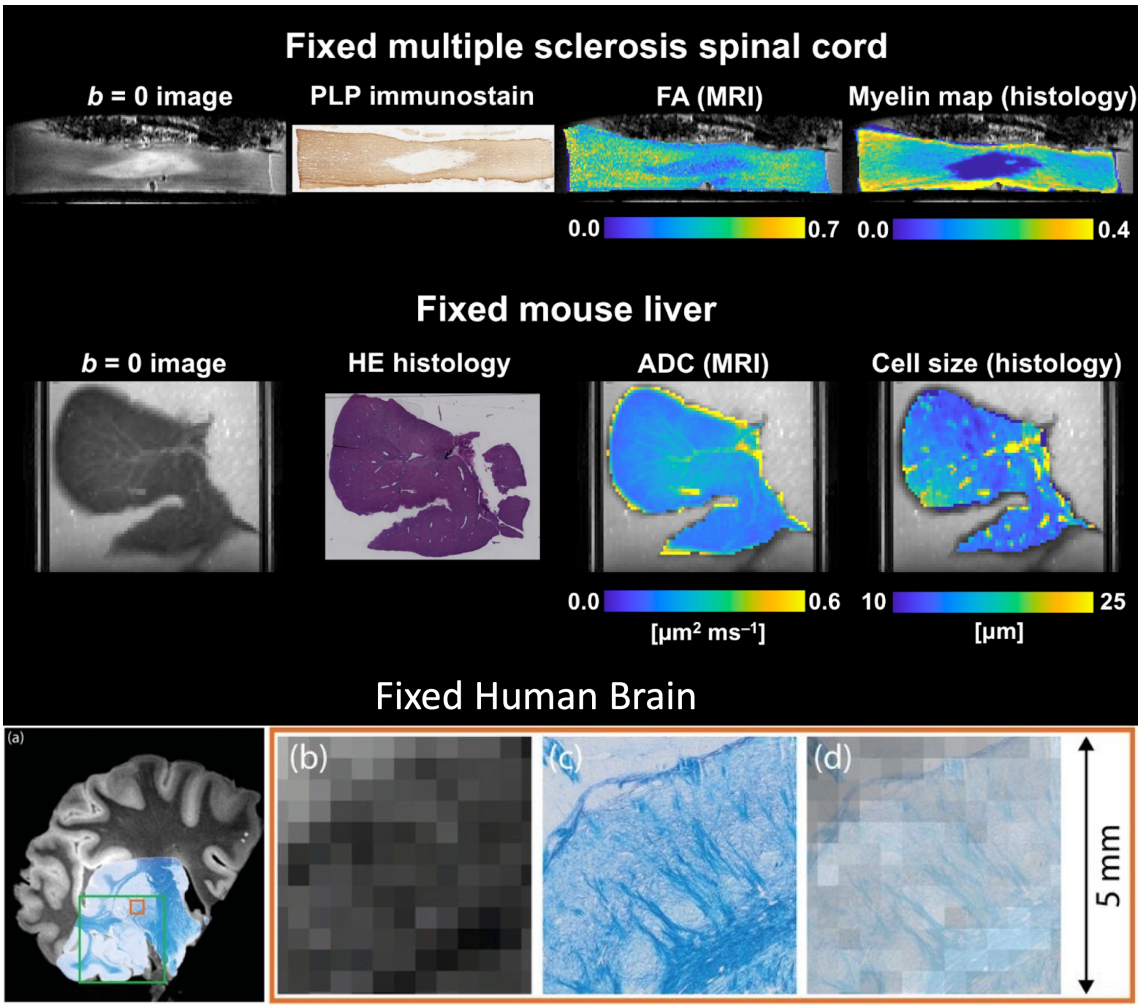


FIGURE 4 Examples of co-localized MRI and histological data. Top: Fixed multiple sclerosis human spinal cord; bottom: Fixed mouse liver. From left to right: $B = 0$ image; whole-sample histological section taken within the tissue corresponding to the MRI slice (proteolipid protein [PLP] immunostain for the spinal cord; hematoxylin and eosin [HE] staining for the mouse liver); dMRI parametric map (fractional anisotropy [FA] for the spinal cord; ADC for the mouse liver); histological parametric maps co-registered to dMRI space (myelin staining fraction for the spinal cord, and volume-weighted cell size statistics for the mouse liver, evaluated within histological image patches matching the in-plane MRI resolution). The data reproduced in this figure with kind permission from C.A.M. Gandini Wheeler-Kingshott, G.C. DeLuca and R. Perez-Lopez refer to previous dMRI studies.[28,77]

4 | COMPARISONS WITH MICROSCOPY

4.1 | Ex vivo MRI-microscopy comparisons

One of the main advantages of the ideal experimental conditions in ex vivo MRI (e.g., lack of motion and limited image distortions; high spatial resolution) is the possibility of deriving detailed microscopy information at accurate radiographic position.[28,73–76] This can then be used to validate MRI maps against microscopy indices quantifying similar biological features, or, more generally, to assess the correlation between MRI markers and a variety of microscopy-derived markers. An example of this is given in Figure 4, illustrating co-localized MRI and histological information from two published studies, i.e. (i) in multiple sclerosis human spinal cord tissue[28] (top), and (ii) in a mouse liver.[77] The figure shows how 2D microscopy from sections cut along a direction that is consistent with the MRI slice direction can be directly compared to MRI markers acquired in the same sample with good MRI-histology alignment,[78] especially if 3D-printed molds customized to the specimen's anatomy are used to guide histological sectioning.[79] 3D microscopy is also possible,[74,80] although it is usually limited to much smaller fields-of-view as compared to sample-wide 2D images, or requires very specialized protocols such as CLARITY.[81]

Irrespective of the chosen method, microscopy images are typically acquired at a resolution that is hundreds or

15222594, 0, Downloaded from https://onlinelibrary.wiley.com/doi/10.1002/mrm.30424 by Ecole Polytech De Montreal, Wiley Online Library on [14/03/2025]. See the Terms and Conditions (https://onlinelibrary.wiley.com/terms-and-conditions) on Wiley Online Library for rules of use; OA articles are governed by the applicable Creative Commons License

thousands of times higher than the MRI voxel size. For example, typical resolutions on 2D slide scanner microscopes used for histology are of the order of 0.25–1.0 μm, while typical ex vivo dMRI resolutions are of the order of 100–500 μm. A common strategy to tackle the resolution mismatch is to combine the microscopy pixels that coincide with a given MR voxel into a "superpixel" or patch that matches the in-plane MRI resolution and derive per-patch descriptors of microstructural properties (e.g., per-patch staining fractions, fiber orientation descriptors, or cell size distribution statistics[27,28,77,82]). This provides microscopy-derived parametric maps at a spatial scale that is comparable to that of diffusion MR images, to enable voxel-by-voxel MRI-microscopy comparisons[83].

For microscopy methods where the brain tissue is first sectioned into thin tissue samples, the resolution mismatch can not only relate to the in-plane resolution, but also to the slice direction: microtome cut thicknesses are of the order of 5–20 μm, while slice thickness in ex vivo dMRI is of the order of 200–1000 μm. This implies that a single microscopy slice only provides a partial picture of the microscopic characteristics underlying an MRI scan, since there are considerable portions of tissue that contribute to the MRI signals but that are not sampled. Better coverage can be achieved by imaging consecutive thin tissue slices that are then co-registered to create a 3D voxel volume,[84] or by using 3D imaging methods such as 3D electron microscopy (EM) methods,[85] confocal Imaging, 3D optical coherence tomography, or x-ray synchrotron-based phase-contrast tomography imaging,[8886,87] and small-angle X-ray scattering (SAXS) tensor tomography[89]. However, some methods are only suitable for imaging smaller tissue samples, precluding whole-brain imaging of larger (e.g., primate) brains. Notably, very high-resolution imaging methods such as electron microscopy are often acquired in 3D from tissue blocks that are smaller than the dMRI voxel resolution, resulting in similar issues.

A further consideration is that microstructure is inherently 3D, consisting of volumetric objects (e.g., cell spheres and fiber cylinders with 3D orientations). However, microscopic 3D images present only a 2D-like projection of the 3D microstructure through the slice thickness. The difference in how a 3D object is represented in different modalities must be carefully accounted for when used for comparison, such as in validation. One approach can be to take the diffusion metric (e.g., a 3D fiber orientation distribution) and similarly project it onto the 2D imaging plane (to create a 2D fiber orientation distribution), facilitating fair MRI-microscopy comparison.[90–93]

In MRI-microscopy comparisons, sensitivity can be demonstrated using natural microstructural variation in healthy tissue, variation between pathological and control tissue, or via animal models in which specific tissue features can be purposefully manipulated (e.g., myelin manipulated through genetic modifications in shiverer mice or through environmental modifications in the cuprizone mouse model). In these cases, the correlation between ex vivo MRI and microscopy need not specifically match MRI voxels to microscopy data and a 1:1 correspondence between these contrasts may not be necessary.

4.2 | Ex vivo MRI and microscopy alignment

There are several ways to align MRI and microscopy for quantitative comparison and validation. An excellent review of challenges and methodologies in registration of MRI to histology is provided in Ref. 94. While not specific to ex vivo diffusion MRI, their recommendations and suggested protocols form the backbone of our review here, given in order of increasing technical difficulty.

First, the most simple, and arguably most common, approach is to manually select corresponding regions of interest in MRI and histology for quantitative analysis[95–97] especially suited for the small field-of-view of electron microscopy and similar techniques that are necessary for axon diameter and volume fraction quantification.[23,31] While no registration is required, it might be time consuming to manually select and delineate regions of interest in both microscopy and MRI, and a perfect correspondence is not guaranteed. For this reason, larger anatomical regions are typically selected from MRI (i.e., genu/body/splenium of corpus callosum, or large hand-drawn region of the cortex).

A second option is to aim to section the tissue specimen in planes parallel to the MR imaging planes. This will facilitate registration of 2D histology to the 2D MRI imaging plane using commonly employed registration packages, enabling a voxel-wise comparison of MRI and histology. A 3D printed mold may be created to facilitate registration. Here, an in vivo or ex vivo structural scan is quickly performed to create a 3D segmentation of the object (i.e., brain, prostate, spinal cord). Then, a mold is designed which not only holds the sample, but also has cutting guides, or slots, for cutting. Some guides may be nicely made to fit within specialized sample holders as well. Further scans can be performed ex vivo, where the FOV may be aligned with the cutting guide, so that there is a direct correspondence between the subsequent 2D histology and a slice (or slices) of the MRI image. This technique has been used for MRI imaging and histology alignment of multiple species and various organs,[79,98–100] but, as of yet, not for diffusion validation directly.

15222594, 0, Downloaded from https://onlinelibrary.wiley.com/doi/10.1002/mrm.30424 by Ecole Polytech De Montreal, Wiley Online Library on [14/03/2025]. See the Terms and Conditions (https://onlinelibrary.wiley.com/terms-and-conditions) on Wiley Online Library for rules of use; OA articles are governed by the applicable Creative Commons License

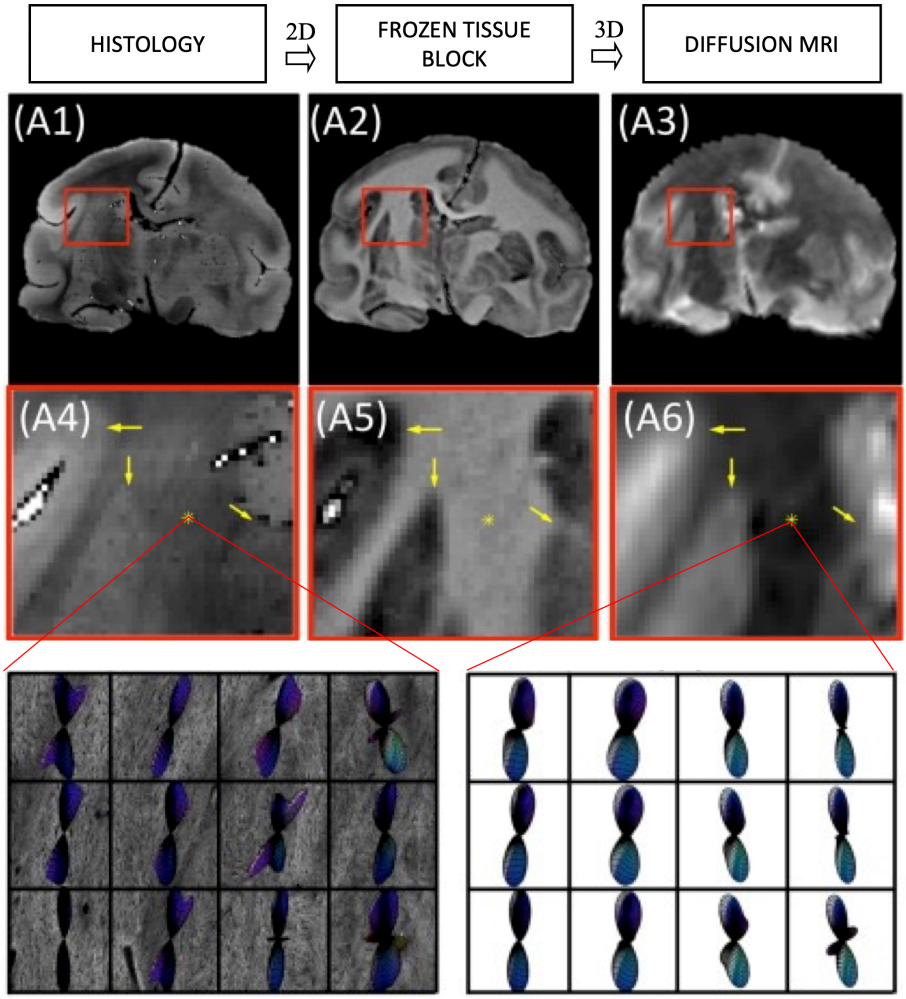


FIGURE 5 Histology to diffusion MRI alignment example using the intermediate modality, block-face images. The 2D histology (A1) can be mapped to specific 2D block-face images (A2), which can be stacked into a 3D volume and mapped directly to 3D diffusion MRI data/derived data (A3). In this example, fiber orientation distribution from histology is aligned with similar measures estimated from diffusion MRI for validation purposes.[75,80] Insets (A4–A5) zoom in to show alignment across modalities, with final panels showing histology-derived (left) and MRI derived (right) fiber orientation distributions.

A third option is to utilize an intermediate modality, usually referred to as block-face images, that are digital photographs of the tissue block as it is being sectioned. These block-face images can be registered individually or first stacked into a 3D volume and registered to the 3D MRI. Because each 2D digital photograph can be mapped directly to a specific 2D histological slice, 2D registration can be performed to align histology to block-face (accounting for non-linear deformations arising from tissue processing), and subsequent 3D registration can be performed to align blockface to MRI (Figure 5). This technique has been performed in humans, mice, and monkeys, with dedicated pipelines and software,[101–104] and has been shown to provide accurate alignment,[105] and used to validate tractography, fiber orientation, and tissue microstructure measures. Registering 2D microscopy directly to 3D MRI is also possible in cases where block-face images were not acquired,[106] though the optimization may be less well constrained.

Despite these options, there are still several challenges associated with MRI and histology alignment. In addition to shrinkage during fixation, tissue distortions including more shrinkage, as well as tearing/folding occur due to sectioning, staining, and mounting procedures (Fox et al. 1985)[154] (or physical distortions during biopsy). This causes both global distortions (global shrinkage), discontinuous distortions (separated tissue segments or parts of the brain, i.e., hemispheres), and also highly localized distortions (tearing, folding, and differential distortions between tissue types). While approaches to overcome this may include interactive or manual delineation of tears (Breen et al. 2005),[103,155] piecewise or hemi-rigid transformations (Pitiot et al. 2006; Dauguet et al. 2007),[156,157] and block-face images above, this is still an open challenge in the field where we envision open-sourced configurable, yet automated, registration for robust and reproducible MRI-histology registration (Huszar et al. 2023).[158]

We also note that, in some special cases, especially with small samples imaged using planar surface coils, the entire RF coil, holder, and sample can be removed for optical microscopy, providing a direct comparison as demonstrated on onion plant cells[112] and in mammalian brain slices (including human[97]), and muscle fibers.[113–117] Examples of this approach on a myelin-stained human

15222594, 0, Downloaded from https://onlinelibrary.wiley.com/doi/10.1002/mrm.30424 by Ecole Polytech De Montreal, Wiley Online Library on [14/03/2025]. See the Terms and Conditions (https://onlinelibrary.wiley.com/terms-and-conditions) on Wiley Online Library for rules of use; OA articles are governed by the applicable Creative Commons License

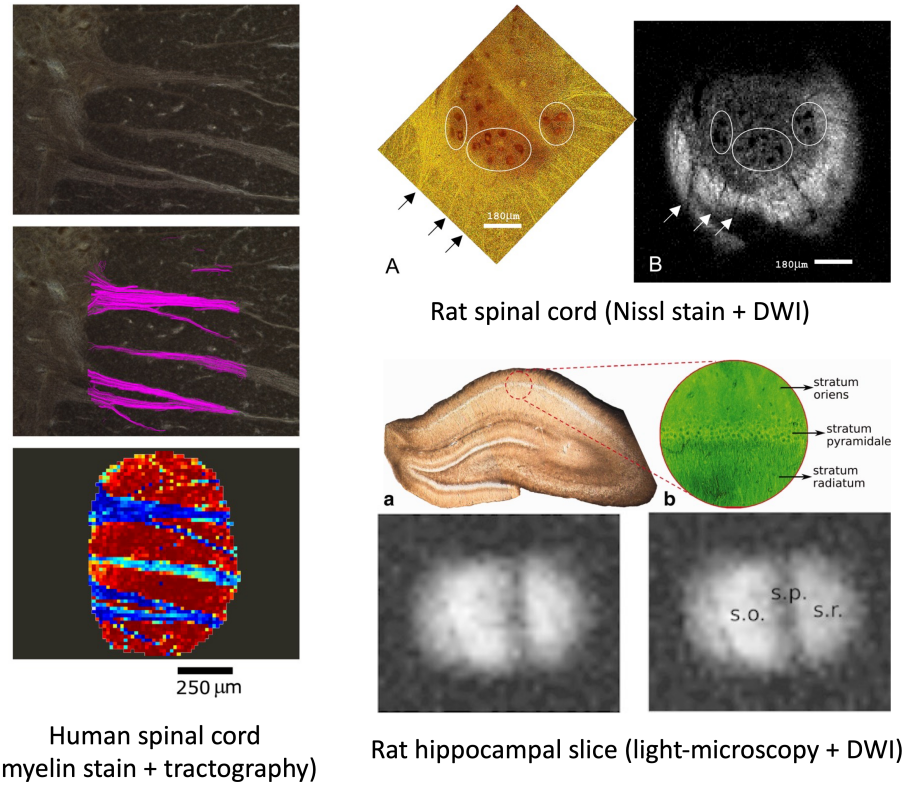


FIGURE 6 Examples of direct imaging of histological slices. (Left) A Black-Gold II stained histology (myelin-stain) was directly imaged in a microsurface coil with in-plane resolution of 15.6um. Tractography and red-green-blue orientation maps are shown overlaid on myelin stain. (Top right) a 25 μm-thick Nissl-stained rat spinal cord tissue was imaged using a microsurface coil at 7.8 μm in-plane resolution with corresponding diffusion weighted image showing excellent correspondence. (Bottom right) A 300 μm-thick rat hippocampal slice is imaged under a light-microscope and imaged using a slide-mounted microsurface coil at 12.5 μm in-plane resolution to study the microstructural effects of diffusion times and *b*-values. Images reproduced from[97] (left),[115] (top right),[117] (bottom right).

spinal cord, Nissl-stained rat spinal cord, and rat hippocampal slice (with light microscopy) are shown in Figure 6.

4.3 | Optical imaging for validation

4.3.1 | Histology

Histological staining is commonly used to visualize specific tissue features at μm-resolution. Ex vivo tissue is first sectioned into thin slices (typically ~5–10 μm), mounted onto glass slides and chemically stained. Many stains exist that target and visualize different tissue features. For example, there are common stains for myelin (e.g., PLP, Luxol fast blue or Gallyas/Bodian silver stains), Nissl or cell bodies (Cresyl violet, Golgi), neurofilaments (SMI-312), astrocytes (glial fibrillary acidic protein [GFAP]), microglia (*Iba*1), and many others. Some stains are chemical while others use antibodies to target specific proteins, known as immunohistochemistry. Stained slides are then imaged using optical microscopy with μm or sub-μm resolution where slide scanners are typically used for high-throughput 2D imaging. Digitized histology can be analyzed to extract microstructural metrics related to, for example, cell density, size, or the degree of axon myelination (via stain segmentation[118]) or fiber orientations (via structure tensor analysis[93,119]). The image processing involved needs to account for considerations that make stain (optical) density semi-quantitative: the stain density may not scale linearly with the antibody density and slides can suffer from artifactual staining variations both within and between slides. After processing, summary measures such as the cell count, the distribution of cell size, the number of stained pixels (stained area fraction) or the fiber orientation distribution can then be calculated over a local neighborhood and compared to dMRI-equivalents across regions of interest or on a voxel-wise basis. To separate sensitivity (showing a MR parameter correlates with some histology metric) from specificity (showing a MR parameter is selectively related to a single change in the tissue), multiple stains may be acquired and simultaneously analyzed to account for microstructural covariance across voxels/regions.[118]

Histology (or immunohistochemistry) can also be combined with chemical tracers to enable precision mapping of axon trajectories from cortical regions of interest.[120] This form of neuroanatomical tract tracing provides "gold standard" estimates of brain connectivity that can be used to validate dMRI-based tractography (Figure 7). Tracer molecules are first surgically injected into a cortical region of interest where the tracer is taken up by neurons and actively transported along the axon, from the cell body to the axon terminals (anterograde tracers) or from the axon terminals to the cell body (retrograde tracers). Several weeks post-surgery, the animal is

15222594, 0, Downloaded from https://onlinelibrary.wiley.com/doi/10.1002/mrm.30424 by Ecole Polytech De Montreal, Wiley Online Library on [14/03/2025]. See the Terms and Conditions (https://onlinelibrary.wiley.com/terms-and-conditions) on Wiley Online Library for rules of use; OA articles are governed by the applicable Creative Commons License

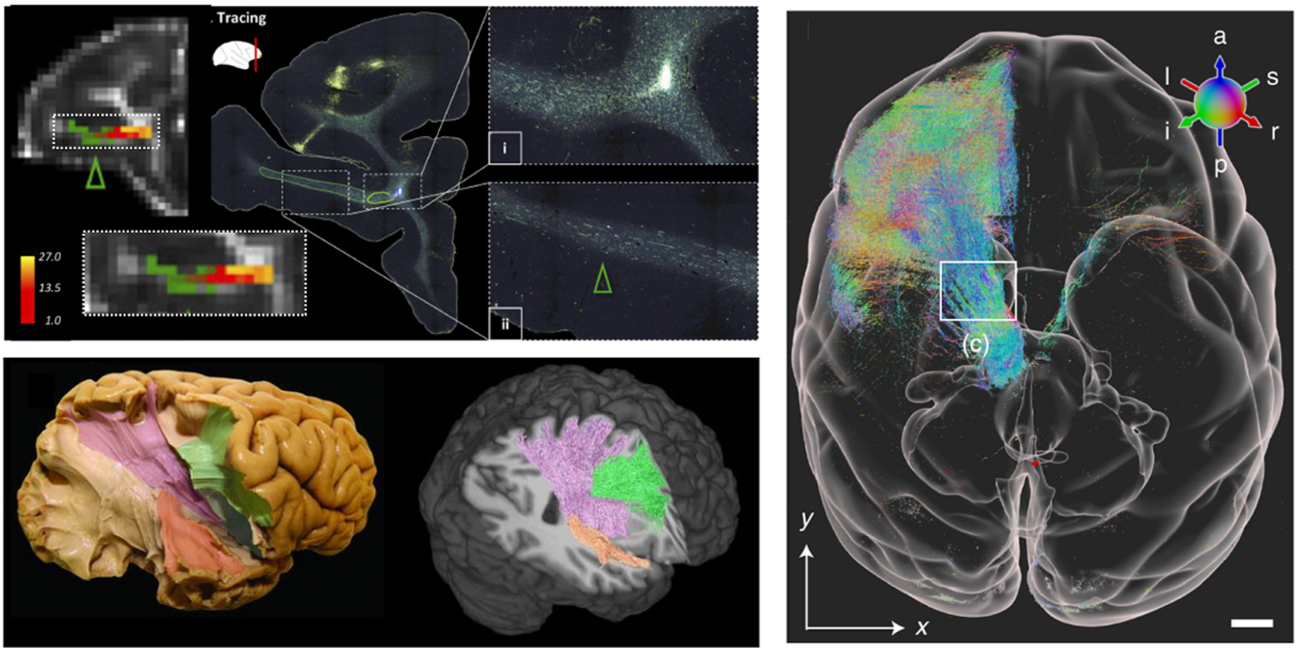


FIGURE 7 Left: Tractography validation via anatomical tracers (top,[122]) and microdissection (bottom,[123]). Right: Recent advances in high throughput 3D imaging of anatomical tracers facilitates the tracking of single neurons, here projecting from the medial dorsal nucleus of the thalamus.[124]

then sacrificed and the tissue sectioned and stained to visualize tracer deposition (i.e., stained cell bodies and axon trajectories) in the tissue. Sections sampled across the brain can then be digitized and combined, to map cortical–cortical or cortical–subcortical connectivity (i.e., injection/termination points), or create a 3D mask of axon projections across the brain. Tracers have been used extensively in animal models such as non-human primates and mice. However, tracers are typically limited to only one or two injection sites per animal, often requiring information to be combined across multiple animals, and tracers cannot be used in humans. Though it is possible to implant similar dyes in postmortem human samples,[121] it can take a prohibitively long time for the dye to travel without active transport, meaning this method is only rarely used. Alternative tract-validation methods include gross white matter dissection, where fixed ex vivo tissue is first frozen and thawed (Kingler's technique) before being surgically dissected to reveal white matter fiber bundles,[120] or comparisons of fiber orientations and downstream tractography from structure tensor outputs, or orientation-sensitive microscopy such as polarized light imaging (PLI), PS-OCT, SLI, or SAXS, as described below and illustrated in Figure 8.

4.3.2 | Fluorescence microscopy and tissue clearing

Fluorescence microscopy can similarly be used to identify specific tissue features with high resolution for single-cell-resolution imaging and analysis. Here, tissue is stained using fluorescent dyes, or animals (e.g., mice) can be genetically engineered to express fluorescent proteins (e.g., using the Brainbow technique (Livet et al. 2007)),[159] eliminating the need for staining. Samples are then imaged often via more advanced optical methods such as confocal microscopy, light-sheet microscopy, two-photon or super-resolution imaging. Multiple fluorophores can be labeled within the same tissue sample for co-localization of multiple tissue features, with the benefit that fluorescence can be directly related to fluorophore concentration given certain conditions, making the method often more quantitative than histological staining. Combining fluorescence with z-stack imaging, cellular morphologies and fiber orientations can be visualized in 3D for comparisons with dMRI.[74,75,80]

Larger tissue sections (~mm^3) can be imaged in 3D at depth by first optically clearing the tissue, for example, via CLARITY.[128] In tissue clearing, lipids are removed from

15222594, 0, Downloaded from https://onlinelibrary.wiley.com/doi/10.1002/mrm.30424 by Ecole Polytech De Montreal, Wiley Online Library on [14/03/2025]. See the Terms and Conditions (https://onlinelibrary.wiley.com/terms-and-conditions) on Wiley Online Library for rules of use; OA articles are governed by the applicable Creative Commons License

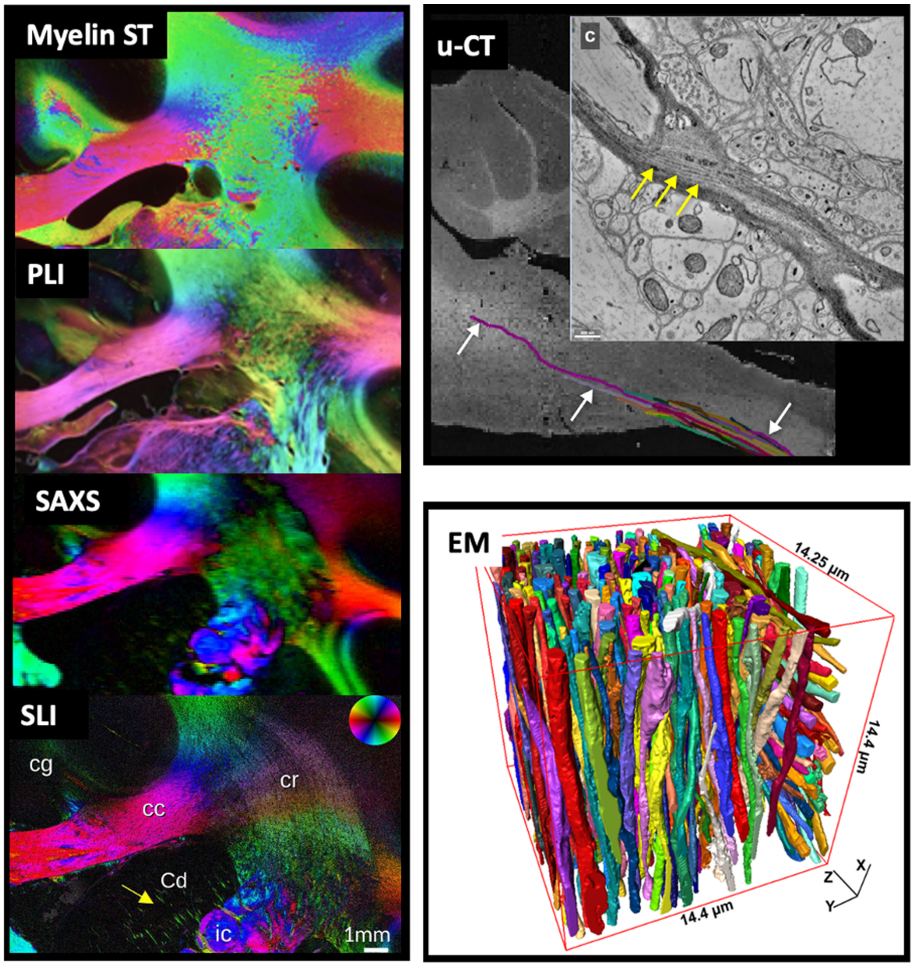


FIGURE 8 Fiber orientations extracted from various microscopy modalities can be used to validate biophysical models or fiber reconstruction methods in diffusion MRI. These modalities include structure tensor analysis of histological sections (myelin ST[106]) and polarized light imaging (PLI[106]), small angle x-ray scattering (SAXS[125]) and scattered light imaging (SLI[125]), micro-CT (u-CT[87]), and EM.[126]

the tissue such that the sample becomes optically transparent, facilitating 3D tissue imaging without sectioning. Penetration issues mean it can be challenging to both clear and label larger samples, though advancements in sample processing are ongoing.[129] Nonetheless, fiber orientations from cleared tissue have been successfully compared to diffusion MRI in both human and primate blocks of $10 \times 10 \times 0.5\,mm^3$,[130] and the contributions to DTI of different cell types, myelin and fiber coherence disentangled in whole-brain mouse data.[131,132]

4.3.3 | Label-free imaging techniques

Label-free imaging methods utilize the intrinsic optical properties of tissue to generate contrast, without additional (exogenous) stains or dyes. Several techniques such as optical coherence tomography (OCT) and scattered light imaging (SLI) use the reflectance or scattering of light from tissue structures to drive contrast in the image. Analogous to ultrasound, OCT[133] uses an optical interferometer to obtain 3D depth-resolved images of reflected light at µm-resolution <~100 µm deep (depending on the sample). The top face of the sample is first imaged and then removed in situ (e.g., using a vibratome), and the process is repeated. This results in well-aligned images without the need for complex post-hoc registration. In comparison, scattered light does not image at depth but illuminates the sample from different angles (typically from below, with light then transmitted through the sample) to estimate fiber orientations with an in-plane resolution of >6.5 µm.[125,134] The primary benefit of SLI over other methods lies in its ability to estimate multiple orientations per pixel in crossing fiber regions. Polarization sensitive methods such as PLI or polarization-sensitive OCT (PS-OCT) use the birefringent properties of the tissue to estimate orientational information (the optic axis) with micron-scale resolution.[40] As tissue birefringence in white matter is primarily related to myelin, fiber orientations can be inferred. The main difference between PLI and PS-OCT lies in the order in which the tissue is sectioned and imaged. In PLI,[135] polarized light is transmitted through unstained tissue slices ~50–100 µm thick, whereas PS-OCT[136] uses reflected light and sections after imaging, as described in OCT above. As with SLI, setups often only provide reliable orientational information within the 2D imaging plane (the "in-plane

15222594, 0, Downloaded from https://onlinelibrary.wiley.com/doi/10.1002/mrm.30424 by Ecole Polytech De Montreal, Wiley Online Library on [14/03/2025]. See the Terms and Conditions (https://onlinelibrary.wiley.com/terms-and-conditions) on Wiley Online Library for rules of use; OA articles are governed by the applicable Creative Commons License

angle"), though 3D PLI can be achieved, for example, through the use of a tilting sample stage.[135] SLI, PLI, and PS-OCT have all been used to validate orientational information from diffusion MRI[58,92,106,125,137–139] (Figure 8).

4.3.4 | Non-optical techniques

Non-optical techniques can provide benefits such as superior penetration or resolution to the optical methods above. 3D High-resolution X-ray imaging technologies such as X-ray nanoholotomography (XNH), hierarchical phase-contrast tomography (HiP-CT), and small angle X-ray scattering (SAXS)[141,140] can be used to image intact tissue samples at meso-scale resolution without sectioning, allowing 3D descriptions of cellular morphology and organization over considerable fields of view. The tomographic 3D imaging method is analogous to clinical CT, where the 3D volume is constructed from 2D back-projections acquired as the tissue sample is rotated in the x-ray beam.[87] Compared with clinical CT, synchrotron x-ray sources provide more intense and highly collimated and coherent x-rays facilitating sub μm-scale resolution ("μ-CT") specifically essential for phase-contrast imaging. To improve contrast, the tissue block is typically first stained with heavy metals such as osmium, though unstained phase-contrast methods available at synchrotron facilities are also possible[86,142]- allowing large samples, such as whole organs, to be scanned as unembedded, hydrated samples, even when unstained, using phase-contrast methods like HiP-CT.[141] In small angle X-ray scattering (SAXS) tensor tomography (TT-SAXS)[143], 3D fiber orientations can be estimated from diffraction (Bragg) peaks in the X-ray scattering pattern due to the systematically organized myelin layers. 3D SAXS provides a quantitative, myelin-specific signal with 3D fiber orientations and multiple, crossing fiber populations per pixel, though at more meso-scale resolutions of ~100 μm in-plane.[125,144] As x-ray imaging is non-destructive, μ-CT and SAXS can be combined with other contrasts such as electron microscopy or classical histology for multi-modal tissue investigations.[87]

Electron microscopy can provide nano-scale visualizations of heavy metal (typically osmium) stained tissue to describe detailed cellular structures including cellular membranes, individual synapses, myelin lamella or features of the cytoskeleton. Tissue can either be imaged using back-scattered EM and then sectioned, preserving 3D localization of tissue structures, or first sectioned and then imaged and co-registered together (transmission EM), where the latter typically provides superior in-plane resolution.[145] EM samples are typically limited to small tissue blocks (~$50 \times 50 \times 50$ μm), though methods for high throughput, large FOV imaging are being developed.[146]

As contrast in both μ-CT and EM is not cell-type specific, data analysis requires the post-hoc segmentation and identification of different cells or tissue (Figure 8). This can be challenging, though automated segmentation methods will continue to benefit from recent advances in machine/deep learning. EM-dMRI and μ-CT-dMRI comparisons include validating variation in axon diameter across the brain,[28,135-137] the degree of myelination for g-ratio mapping,[138-140] or quantifying intracellular fractions.[95] Further, 3D meshes from EM and μ-CT can be used as inputs for more microstructurally realistic simulations of water diffusion through tissue to investigate how deviations from highly simplistic tissue models favored in diffusion MRI (e.g., complex axon morphologies versus stick-like axons) impact the diffusion signal.[153–155] [156]Due to limited resolution and lack of contrast from relatively unmyelinated, low-diameter axons, μ-CT and EM can be biased toward large diameter axons, which may confound dMRI comparisons[157].

5 | PERSPECTIVES

5.1 | Open science

5.1.1 | Code/software

Challenges with pre-processing and processing pipelines highlighted in the previous sections could start to be overcome through code sharing and harmonization of implementations. Sharing combined knowledge and experience of many groups is valuable as it generates a lower barrier to entry and an excellent opportunity to evaluate robustness and reproducibility. We provide a (non-comprehensive) list of available software dedicated for acquisition and processing ex vivo diffusion MRI data at (https://github.com/Diffusion-MRI/awesome-preclinical-diffusion-mri) where updates on available software and tools can be shared by developers and where users can ask questions/advice for implementation, etc.

5.1.2 | Data sharing & databases

Platforms that could serve as a repository for ex vivo dMRI datasets include OSF, OpenNeuro, Zenodo, NITRC, or other center resources (e.g., US National High Magnetic Field Laboratory). To promote data sharing and reuse, we compiled a (non-comprehensive) list of existing freely shared small-animal or ex vivo diffusion-weighted datasets, available on a public repository: https://github

15222594, 0, Downloaded from https://onlinelibrary.wiley.com/doi/10.1002/mrm.30424 by Ecole Polytech De Montreal, Wiley Online Library on [14/03/2025]. See the Terms and Conditions (https://onlinelibrary.wiley.com/terms-and-conditions) on Wiley Online Library for rules of use; OA articles are governed by the applicable Creative Commons License

.com/Diffusion-MRI/awesome-preclinical-diffusion-mri.git. As for code sharing, the repository will enable a regular update of this database by the community.

5.2 | The future: What should we strive to achieve?

As a field, we should continually strive to achieve reduced barriers to entry for new imaging centers, new scientists, and new industries who aim to use dMRI in a preclinical setting. Toward this end, as a community, we should promote dissemination of knowledge, code, and datasets to achieve high standards of data quality and analysis, reproducibility, transparency, and foster collaborations, as well as reduce globally the time requirements and cost of research in this field. For easier and more direct translatability, direct access to and control over diffusion sequence timings on clinical systems would be a major benefit. A system for more organized sharing of custom sequences for preclinical systems would also lower the barrier for implementation of advanced techniques.

By design, ex vivo dMRI enables a more direct comparison/validation with invasive or destructive techniques such as histological stainings, chemical tracers, or electron microscopy. This potential can be exploited to its fullest to characterize and understand the biology behind a variety of diseases and injuries, thus contributing immensely to the translational value of dMRI.

Notwithstanding, for the translational circle to be complete, more research is needed to bridge ex vivo with in vivo measurements. So far, the extrapolation of ex vivo measurements to their in vivo counterpart has been hampered by open questions regarding the changes that the tissue undergoes during fixation and how those affect NMR-based measurements. Examples include the impact of partial volume effects between tissue types in high spatial resolution (ex vivo) imaging vs. moderate resolution (in vivo) imaging, changes in compartment relaxation times and diffusivities, in membrane permeability, in relative compartment sizes, etc. Tissue fixation techniques such as cryofixation enable electron microscopy imaging of biological tissues where the in vivo structure was preserved to a greater extent that with regular chemical fixation[158] — which would provide a more realistic "ground truth" or comparative method for dMRI-derived in vivo microstructure, and for relative compartment sizes in particular. New preparation techniques have also recently enabled joint imaging using light microscopy (immunofluorescence) and electron microscopy on cryofixed tissue, with full hydration for light microscopy imaging[159]; the exploration of MR imaging of cryofixed rehydrated samples would certainly be worthwhile. Finally, with the advent of 3D large field of view microscopy with potential tissue clearing methods, it may be advantageous to perform direct 3D to 3D registration from histology to MRI for voxel-wise comparison and validation. However, due to large differences in resolution, contrasts, and geometric tissue distortions, substantial work is needed to make these comparisons feasible.

Future work related to preclinical imaging (and not specific to ex vivo) include:

Pre-processing steps are far from being optimized and integrated into a seamless pipeline for dMRI, so an initiative in this direction, ideally for each species, would highly benefit the community. We note this is not unique to ex vivo dMRI, nor preclinical dMRI, as there is no consensus or full understanding of the effects of different steps in preprocessing human in vivo data.

Transparent processing pipelines should also become the norm in the near future, though given the diversity and complexity of possible dMRI analyses, harmonization may be out of reach or even unjustified. We encourage new community members to search for existing tools in our GitHub database and expand/build on that.

New biophysical models of tissue are typically initially tested in a preclinical imaging setting. We underline that the development of new models should uphold high standards in terms of accuracy and precision of microstructural features estimated and be validated using complementary techniques such as light or electron microscopy.

Rather than debate or controversy, most of the lack of tractography guidelines comes from a sparsity of resources dedicated to this application in the animal models. Future work could thus lie in creating resources that allow whole brain tractography in various species, followed by atlas-based labeling and bundle dissection for pathways of interest. As for biophysical models of microstructure, tractography is often validated in a preclinical setting. Thus, another path for future efforts is to understand and quantify differences between tractography and tracer, and to relate these to situations (i.e. tissue complexities such as crossing fibers) that may occur in the human brain.

To remain consistent with b-value units of s/mm^2 typically set at the scanner console and with "common language", we have reported b-values in s/mm^2 and diffusivities in mm^2/s throughout this work. However, we would like to encourage the community to gradually adopt units that are more suitable for dMRI of biological tissue, where diffusion lengths are on the order of a few microns and diffusion times on the order of a few milliseconds. Hence, diffusivities expressed in μm^2/ms and b-values expressed in ms/μm^2 are much more "natural" and enable to juggle numbers close to unity versus thousands (e.g., $b = 1$ ms/μm^2 vs. $b = 1000$ s/mm^2) or decimals (e.g., $D = 1$ μm^2/ms vs. $D = 10^{-3}$ mm^2/s). Some of

15222594, 0, Downloaded from https://onlinelibrary.wiley.com/doi/10.1002/mrm.30424 by Ecole Polytech De Montreal, Wiley Online Library on [14/03/2025]. See the Terms and Conditions (https://onlinelibrary.wiley.com/terms-and-conditions) on Wiley Online Library for rules of use; OA articles are governed by the applicable Creative Commons License

the recent literature on dMRI microstructure models have adopted this new convention, and we hope it will prevail in the near future.

AFFILIATIONS

[1]Radiology and Radiological Sciences, Vanderbilt University Medical Center, Nashville, Tennessee USA

[2]Vanderbilt University Institute of Imaging Science, Vanderbilt University, Nashville, Tennessee USA

[3]Department of Bioengineering, Imperial College London, London, UK

[4]FMRIB Centre, Wellcome Centre for Integrative Neuroimaging, Nuffield Department of Clinical Neurosciences, University of Oxford, Oxford, UK

[5]Radiomics Group, Vall d'Hebron Institute of Oncology, Vall d'Hebron Barcelona Hospital Campus, Barcelona, Spain

[6]Queen Square MS Centre, Queen Square Institute of Neurology, Faculty of Brain Sciences, University College London, London, UK

[7]School of Biomedical Engineering and Imaging Sciences, King's College London, London, England

[8]Champalimaud Research, Champalimaud Foundation, Lisbon, Portugal

[9]Center of Functionally Integrative Neuroscience, Aarhus University, Aarhus, Denmark

[10]Department of Neuroimaging, Institute of Psychiatry, Psychology and Neuroscience, King's College London, London, UK

[11]NatBrainLab, Department of Forensics and Neurodevelopmental Sciences, Institute of Psychiatry, Psychology and Neuroscience, King's College London, London, UK

[12]Russell H. Morgan Department of Radiology and Radiological Science, Johns Hopkins University School of Medicine, Baltimore, Maryland USA

[13]Department of Neurosurgery, School for Mental Health and Neuroscience (MHeNS), Maastricht University Medical Center, Maastricht, The Netherlands

[14]The Queensland Brain Institute, The University of Queensland, Brisbane, Queensland Australia

[15]Melbourne Neuropsychiatry Centre, The University of Melbourne, Parkville, Victoria Australia

[16]Department of Radiology and Imaging Sciences, Indiana University, Bloomington, Indiana USA

[17]Stark Neurosciences Research Institute, Indiana University School of Medicine, Bloomington, Indiana USA

[18]Center for Biomedical Imaging, NYU Grossman School of Medicine, New York, New York USA

[19]Faculty of Psychology and Neuroscience, Maastricht University, Maastricht, Netherlands

[20]Department of Chemical & Biomedical Engineering, FAMU-FSU College of Engineering, Florida State University, Tallahassee, Florida USA

[21]Center for Interdisciplinary Magnetic Resonance, National HIgh Magnetic Field Laboratory, Tallahassee, Florida USA

[22]Department of Neuropsychology, Max Planck Institute for Human Cognitive and Brain Sciences, Leipzig, Germany

[23]USC Stevens Neuroimaging and Informatics Institute, Keck School of Medicine of USC, University of Southern California, Los Angeles, California USA

[24]Department of Neuroscience, Center for Magnetic Resonance Research, University of Minnesota, Minneapolis, Minnesota USA

[25]Aix Marseille Univ, CNRS, CRMBM, Marseille, France

[26]Bio-Imaging Lab, Faculty of Pharmaceutical, Biomedical and Veterinary Sciences, University of Antwerp, Antwerp, Belgium

[27]μNEURO Research Centre of Excellence, University of Antwerp, Antwerp, Belgium

[28]Wellcome Centre for Integrative Neuroimaging, FMRIB, Nuffield Department of Clinical Neurosciences, University of Oxford, Oxford, UK

[29]Department of Radiology, Lausanne University Hospital and University of Lausanne, Lausanne, Switzerland

[30]imec Vision Lab, Department of Physics, University of Antwerp, Antwerp, Belgium

[31]Lab for Equilibrium Investigations and Aerospace, Department of Physics, University of Antwerp, Antwerp, Belgium

[32]Department of Chemical and Biological Physics, Weizmann Institute of Science, Rehovot, Israel

[33]Division of Child Development & Growth, Department of Pediatrics, Gynaecology & Obstetrics, School of Medicine, Université de Genève, Genève, Switzerland

[34]Department of Radiology, Cumming School of Medicine, University of Calgary, Calgary, Alberta Canada

[35]Hotchkiss Brain Institute, Cumming School of Medicine, University of Calgary, Calgary, Alberta Canada

[36]Alberta Children's Hospital Research Institute, Cumming School of Medicine, University of Calgary, Calgary, Alberta Canada

[37]Department of Electrical and Computer Engineering, Vanderbilt University, Nashville, Tennessee USA

[38]Department of Radiology and Radiological Sciences, Vanderbilt University Medical Center, Nashville, Tennessee USA

[39]Medical University of South Carolina, Charleston, South Carolina USA

[40]National Imaging Facility, The University of Queensland, Brisbane, Queensland Australia

[41]Department of Forensic and Neurodevelopmental Sciences, King's College London, London, UK

[42]Laboratory on Quantitative Medical Imaging, NIBIB, National Institutes of Health, Bethesda, Maryland USA

[43]Department of Computer Science, University College London, London, UK

[44]PROVIDI Lab, Image Sciences Institute, University Medical Center Utrecht, Utrecht, The Netherlands

[45]Biomedical Engineering, Vanderbilt University, Nashville, Tennessee USA

[46]Sherbrooke Connectivity Imaing Lab (SCIL), Computer Science Department, Université de Sherbrooke, Sherbrooke, Quebec Canada

[47]Imeka Solutions, Sherbrooke, Quebec Canada

[48]Department of Radiology and Biomedical Imaging, University of California San Francisco, San Francisco, California USA

[49]Department of Radiology, Perelman School of Medicine, University of Pennsylvania, Philadelphia, Pennsylvania USA

[50]Department of Radiology, Children's Hospital of Philadelphia, Philadelphia, Pennsylvania USA

[51]Centre for NeuroImaging Research (CENIR), Inserm U 1127, CNRS UMR 7225, Sorbonne Université, Paris, France

15222594, 0, Downloaded from https://onlinelibrary.wiley.com/doi/10.1002/mrm.30424 by Ecole Polytech De Montreal, Wiley Online Library on [14/03/2025]. See the Terms and Conditions (https://onlinelibrary.wiley.com/terms-and-conditions) on Wiley Online Library for rules of use; OA articles are governed by the applicable Creative Commons License

[52]Paris Brain Institute, Paris, France

[53]Department of Pediatrics, University of California Irvine, Irvine, California USA

[54]Preclinical and Translational Imaging Center, University of California Irvine, Irvine, California USA

[55]Department of Radiology, Weill Cornell Medical College, New York, New York USA

[56]Key Laboratory for Biomedical Engineering of Ministry of Education, College of Biomedical Engineering & Instrument Science, Zhejiang University, Hangzhou, China

[57]CEA, DRF, JOLIOT, NeuroSpin, Gif-sur-Yvette, France

[58]Université Paris-Saclay, Gif-sur-Yvette, France

[59]Department of Neuroscience, University of Florida, Gainesville, Florida USA

[60]McKnight Brain Institute, University of Florida, Gainesville, Florida USA

[61]National High Magnetic Field Laboratory, Tallahassee, Florida USA

[62]NeuroSpin, UMR CEA/CNRS 9027, Paris-Saclay University, Gif-sur-Yvette, France

[63]Department of Radiology, New York University Grossman School of Medicine, New York, New York USA

[64]Interdisciplinary Institute of Neuroscience and Technology, School of Medicine, Zhejiang University, Hangzhou, China

[65]Frontier Center of Brain Science and Brain-machine Integration, Zhejiang University,

[66]Department of Molecular Biology, Institute of Basic Medical Sciences, University of Oslo, Oslo, Norway

[67]Department of Radiology, New York University School of Medicine, New York, New York USA

[68]Danish Research Centre for Magnetic Resonance, Centre for Functional and Diagnostic Imaging and Research, Copenhagen University Hospital Amager & Hvidovre, Hvidovre, Denmark

[69]Department of Applied Mathematics and Computer Science, Technical University of Denmark, Kongens Lyngby, Denmark

[70]Duke Center for In Vivo Microscopy, Department of Radiology, Duke University, Durham, North Carolina USA

[71]Department of Biomedical Engineering, Duke University, Durham, North Carolina USA

[72]NeuroPoly Lab, Institute of Biomedical Engineering, Polytechnique Montreal, Montreal, Quebec Canada

[73]Functional Neuroimaging Unit, CRIUGM, University of Montreal, Montreal, Quebec Canada

[74]Mila - Quebec AI Institute, Montreal, Quebec Canada

[75]Department of Neurosurgery, Medical College of Wisconsin, Milwaukee, Wisconsin USA

[76]Clement J Zablocki VA Medical Center, Milwaukee, Wisconsin USA

[77]CIBM Center for Biomedical Imaging, Ecole Polytechnique Fédérale de Lausanne, Lausanne, Switzerland

ACKNOWLEDGMENTS

The authors acknowledge financial support from: the National Institutes of Health (K01EB032898, R01AG057991, R01NS125020, R01EB017230, R01EB019980, R01EB031954, R01CA160620, R01NS109090), the National Institute of Biomedical Imaging and Bioengineering (R01EB031765, R56EB031765), the National Institute on Drug Abuse (P30DA048742), the Secretary of Universities and Research (Government of Catalonia) Beatriu de Pinós postdoctoral fellowship (2020 BP 00117), "la Caixa" Foundation Junior Leader fellowship (LCF/BQ/PR22/11920010), the Research Foundation Flanders (FWO: 12M3119N), the Belgian Science Policy Prodex (Grant ISLRA 2009–1062), the μNEURO Research Center of Excellence of the University of Antwerp, the Institutional research chair in Neuroinformatics (Sherbrooke, Canada), the NSERC Discovery Grant, the European Research Council Consolidator grant (101044180), the Canada Research Chair in Quantitative Magnetic Resonance Imaging [950-230815], the Canadian Institute of Health Research [CIHR FDN-143263], the Canada Foundation for Innovation [32454, 34824], the Fonds de Recherche du Québec - Santé [322736], the Natural Sciences and Engineering Research Council of Canada [RGPIN-2019-07244], the Canada First Research Excellence Fund (IVADO and TransMedTech), the Courtois NeuroMod project, the Quebec BioImaging Network [5886, 35450], the Mila - Tech Transfer Funding Program and the Swiss National Science Foundation (Eccellenza Fellowship PCEFP2_194260), the Wellcome Trust (202788/Z/16/A, 203139/Z/16/Z and 203139/A/16/Z).

DATA AVAILABILITY STATEMENT

We provide a (non-comprehensive) list of available software dedicated for acquisition and processing ex vivo diffusion MRI data at (https://github.com/Diffusion-MRI/awesome-preclinical-diffusion-mri) where updates on available software and tools can be shared by developers and where users can ask questions/advice for implementation, etc.

ORCID

Kurt G. Schilling https://orcid.org/0000-0003-3686-7645

Ileana O. Jelescu https://orcid.org/0000-0002-3664-0195

REFERENCES

1. Jelescu IO, Grussu F, Ianus A, Hansen B. Recommendations and guidelines from the ISMRM Diffusion Study Group for preclinical diffusion MRI: part 1–in vivo small-animal imaging. *arXiv preprint arXiv*. 2022. https://arxiv.org/abs/2209.12994
2. Mesri HY, David S, Viergever MA, Leemans A. The adverse effect of gradient nonlinearities on diffusion MRI: from voxels to group studies. *Neuroimage*. 2020;205:116127.
3. Vos SB, Tax CMW, Luijten PR, Ourselin S, Leemans A, Froeling M. The importance of correcting for signal drift in diffusion MRI. *Magn Reson Med*. 2017;77:285-299. doi:10.1002/mrm.26124

15222594, 0, Downloaded from https://onlinelibrary.wiley.com/doi/10.1002/mrm.30424 by Ecole Polytech De Montreal, Wiley Online Library on [14/03/2025]. See the Terms and Conditions (https://onlinelibrary.wiley.com/terms-and-conditions) on Wiley Online Library for rules of use; OA articles are governed by the applicable Creative Commons License

4. Jeurissen B, Leemans A, Sijbers J. Automated correction of improperly rotated diffusion gradient orientations in diffusion weighted MRI. *Med Image Anal*. 2014; 18:953-962.
5. Schilling KG, Yeh FC, Nath V, et al. A fiber coherence index for quality control of B-table orientation in diffusion MRI scans. *Magn Reson Imaging*. 2019;58:82-89.
6. Tournier JD, Smith R, Raffelt D, et al. MRtrix3: a fast, flexible and open software framework for medical image processing and visualisation. *Neuroimage*. 2019;202:116137.
7. Messinger A, Sirmpilatze N, Heuer K, et al. A collaborative resource platform for non-human primate neuroimaging. *Neuroimage*. 2021;226:117519.
8. Friedel M, van Eede MC, Pipitone J, Chakravarty MM, Lerch JP. Pydpiper: a flexible toolkit for constructing novel registration pipelines. *Front Neuroinform*. 2014;8:67.
9. Manjón JV, Coupé P, Concha L, Buades A, Louis Collins D, Robles M. Diffusion weighted image denoising using overcomplete local PCA. *PLoS One*. 2013;8:e73021. doi:10.1371/journal.pone.0073021
10. Veraart J, Novikov DS, Christiaens D, Ades-Aron B, Sijbers J, Fieremans E. Denoising of diffusion MRI using random matrix theory. *Neuroimage*. 2016;142:394-406.
11. Moeller S, Pisharady PK, Ramanna S, et al. NOise reduction with DIstribution Corrected (NORDIC) PCA in dMRI with complex-valued parameter-free locally low-rank processing. *Neuroimage*. 2021;226:117539.
12. Rudin LI, Osher S, Fatemi E. Nonlinear total variation based noise removal algorithms. *Phys D: Nonlinear Phenomena*. 1992;60:259-268. doi:10.1016/0167-2789(92)90242-f
13. Coupe P, Yger P, Prima S, Hellier P, Kervrann C, Barillot C. An optimized blockwise nonlocal means denoising filter for 3-D magnetic resonance images. *IEEE Trans Med Imaging*. 2008;27:425-441. doi:10.1109/tmi.2007.906087
14. Manzano-Patron JP, Moeller S, Andersson JLR, Ugurbil K, Yacoub E, Sotiropoulos SN. Denoising diffusion MRI: considerations and implications for analysis. *Imaging Neuroscience*. 2024: 1-29. doi: 10.1162/imag_a_00060
15. Dyrby TB, Sogaard LV, Hall MG, Ptito M, Alexander DC. Contrast and stability of the axon diameter index from microstructure imaging with diffusion MRI. *Magn Reson Med*. 2013;70:711-721.
16. Kellner E, Dhital B, Kiselev VG, Reisert M. Gibbs-ringing artifact removal based on local subvoxel-shifts. *Magn Reson Med*. 2016;76:1574-1581.
17. Lee HH, Novikov DS, Fieremans E. Removal of partial Fourier-induced Gibbs (RPG) ringing artifacts in MRI. *Magn Reson Med*. 2021;86:2733-2750.
18. Bautista T, O'Muircheartaigh J, Hajnal JV, Tournier JD. Removal of Gibbs ringing artefacts for 3D acquisitions using subvoxel shifts. *Proceedings of the International Society for Magnetic Resonance in Medicine*; 2021. https://archive.ismrm.org/2021/3535.html
19. Ades-Aron B, Veraart J, Kochunov P, et al. Evaluation of the accuracy and precision of the diffusion parameter EStImation with Gibbs and NoisE removal pipeline. *Neuroimage*. 2018;183:532-543.
20. Koay CG, Basser PJ. Analytically exact correction scheme for signal extraction from noisy magnitude MR signals. *J Magn Reson*. 2006;179:317-322.
21. Kiselev VG. The cumulant expansion: an overarching mathematical framework for understanding diffusion NMR. In: Derek K. Jones, PhD (ed.), *Diffusion MRI: Theory, Methods, and Applications*. (2010. online edn, Oxford Academic, 1 Sept. 2012). https://doi.org/10.1093/med/9780195369779.003.0010, Accessed January 25, 2025.
22. Zhang H, Schneider T, Wheeler-Kingshott CA, Alexander DC. NODDI: practical in vivo neurite orientation dispersion and density imaging of the human brain. *Neuroimage*. 2012;61:1000-1016. doi:10.1016/j.neuroimage.2012.03.072
23. Alexander DC, Hubbard PL, Hall MG, et al. Orientationally invariant indices of axon diameter and density from diffusion MRI. *Neuroimage*. 2010;52:1374-1389.
24. Tax CMW, Szczepankiewicz F, Nilsson M, Jones DK. The dot-compartment revealed? Diffusion MRI with ultra-strong gradients and spherical tensor encoding in the living human brain. *Neuroimage*. 2020;210:116534.
25. Dhital B, Kellner E, Kiselev VG, Reisert M. The absence of restricted water pool in brain white matter. *Neuroimage*. 2018;182:398-406.
26. Panagiotaki E, Schneider T, Siow B, Hall MG, Lythgoe MF, Alexander DC. Compartment models of the diffusion MR signal in brain white matter: a taxonomy and comparison. *Neuroimage*. 2012;59:2241-2254.
27. Veraart J, Nunes D, Rudrapatna U, et al. Noninvasive quantification of axon radii using diffusion MRI. *Elife*. 2020;9:e49855.
28. Grussu F, Schneider T, Tur C, et al. Neurite dispersion: a new marker of multiple sclerosis spinal cord pathology? *Ann Clin Transl Neurol*. 2017;4:663-679.
29. Stanisz GJ, Szafer A, Wright GA, Henkelman RM. An analytical model of restricted diffusion in bovine optic nerve. *Magn Reson Med*. 1997;37:103-111.
30. Fieremans E, Jensen JH, Helpern JA. White matter characterization with diffusional kurtosis imaging. *Neuroimage*. 2011;58:177-188.
31. Kelm ND, West KL, Carson RP, Gochberg DF, Ess KC, Does MD. Evaluation of diffusion kurtosis imaging in ex vivo hypomyelinated mouse brains. *Neuroimage*. 2016;124:612-626.
32. Manivannan A, Foley LM, Hitchens TK, Rattray I, Bates GP, Modo M. Ex vivo 100 μm isotropic diffusion MRI-based tractography of connectivity changes in the end-stage R6/2 mouse model of Huntington's disease. *Neuroprotection*. 2023;1:66-83.
33. Warrington S, Bryant KL, Khrapitchev AA, et al. XTRACT - standardised protocols for automated tractography in the human and macaque brain. *Neuroimage*. 2020;217:116923.
34. Aggarwal M, Zhang J, Pletnikova O, Crain B, Troncoso J, Mori S. Feasibility of creating a high-resolution 3D diffusion tensor imaging based atlas of the human brainstem: a case study at 11.7 T. *Neuroimage*. 2013;74:117-127.
35. Neher P, Stieltjes B, Wolf I, Meinzer HP, Maier-Hein K. Analysis of tractography biases introduced by anisotropic voxels; 2013.
36. Moldrich RX, Pannek K, Hoch R, Rubenstein JL, Kurniawan ND, Richards LJ. Comparative mouse brain tractography of diffusion magnetic resonance imaging. *Neuroimage*. 2010;51:1027-1036.
37. Delettre C, Messé A, Dell LA, et al. Comparison between diffusion MRI tractography and histological tract-tracing of cortico-cortical structural connectivity in the ferret brain. *Netw Neurosci*. 2019;3:1038-1050.

15222594, 0, Downloaded from https://onlinelibrary.wiley.com/doi/10.1002/mrm.30424 by Ecole Polytech De Montreal, Wiley Online Library on [14/03/2025]. See the Terms and Conditions (https://onlinelibrary.wiley.com/terms-and-conditions) on Wiley Online Library for rules of use; OA articles are governed by the applicable Creative Commons License

38. Schilling KG, Gao Y, Stepniewska I, Janve V, Landman BA, Anderson AW. Anatomical accuracy of standard-practice tractography algorithms in the motor system - a histological validation in the squirrel monkey brain. *Magn Reson Imaging*. 2019;55:7-25.
39. Schilling K, Gao Y, Janve V, Stepniewska I, Landman BA, Anderson AW. Confirmation of a gyral bias in diffusion MRI fiber tractography. *Hum Brain Mapp*. 2018;39:1449-1466.
40. Thomas C, Ye FQ, Irfanoglu MO, et al. Anatomical accuracy of brain connections derived from diffusion MRI tractography is inherently limited. *Proc Natl Acad Sci U S A*. 2014;111:16574-16579.
41. Girard G, Caminiti R, Battaglia-Mayer A, et al. On the cortical connectivity in the macaque brain: a comparison of diffusion tractography and histological tracing data. *Neuroimage*. 2020;221:117201.
42. Ambrosen KS, Eskildsen SF, Hinne M, et al. Validation of structural brain connectivity networks: the impact of scanning parameters. *Neuroimage*. 2020;204:116207.
43. Knösche TR, Anwander A, Liptrot M, Dyrby TB. Validation of tractography: comparison with manganese tracing. *Hum Brain Mapp*. 2015;36:4116-4134.
44. Basser PJ, Mattiello J, LeBihan D. Estimation of the effective self-diffusion tensor from the NMR spin echo. *J Magn Reson B*. 1994;103:247-254.
45. Tournier JD, Calamante F, Connelly A. Robust determination of the fibre orientation distribution in diffusion MRI: non-negativity constrained super-resolved spherical deconvolution. *Neuroimage*. 2007;35:1459-1472.
46. Behrens TEJ, Berg HJ, Jbabdi S, Rushworth MFS, Woolrich MW. Probabilistic diffusion tractography with multiple fibre orientations: what can we gain? *Neuroimage*. 2007;34:144-155.
47. Tuch DS. Q-ball imaging. *Magn Reson Med*. 2004;52:1358-1372.
48. Jbabdi S, Sotiropoulos SN, Savio AM, Graña M, Behrens TEJ. Model-based analysis of multishell diffusion MR data for tractography: how to get over fitting problems. *Magn Reson Med*. 2012;68:1846-1855.
49. Dell'Acqua F, Scifo P, Rizzo G, et al. A modified damped Richardson–Lucy algorithm to reduce isotropic background effects in spherical deconvolution. *Neuroimage*. 2010;49:1446-1458.
50. Jeurissen B, Tournier JD, Dhollander T, Connelly A, Sijbers J. Multi-tissue constrained spherical deconvolution for improved analysis of multi-shell diffusion MRI data. *Neuroimage*. 2014;103:411-426.
51. Dhollander T, Connelly A. A novel iterative approach to reap the benefits of multi-tissue CSD from just single-shell (+b=0) diffusion MRI data. In: *Conference: 24th International Society of Magnetic Resonance in Medicine*; 2016. https://www.researchgate.net/profile/Thijs-Dhollander/publication/301766619_A_novel_iterative_approach_to_reap_the_benefits_of_multi-tissue_CSD_from_just_single-shell_b0_diffusion_MRI_data/links/5726b0e608aee491cb3f111d/A-novel-iterative-approach-to-reap-the-benefits-of-multi-tissue-CSD-from-just-single-shell-b0-diffusion-MRI-data.pdf. Accessed January 17, 2024
52. Bryant KL, Ardesch DJ, Roumazeilles L, et al. Diffusion MRI data, sulcal anatomy, and tractography for eight species from the Primate Brain Bank. *Brain Struct Funct*. 2021;226:2497-2509.
53. Berns GS, Cook PF, Foxley S, Jbabdi S, Miller KL, Marino L. Diffusion tensor imaging of dolphin brains reveals direct auditory pathway to temporal lobe. *Proc Biol Sci*. 1811;2015:20151203.
54. Cook PF, Berns GS, Colegrove K, Johnson S, Gulland F. Post-mortem DTI reveals altered hippocampal connectivity in wild sea lions diagnosed with chronic toxicosis from algal exposure. *J Comp Neurol*. 2018;526:216-228.
55. Berns GS, Ashwell KWS. Reconstruction of the cortical maps of the Tasmanian tiger and comparison to the Tasmanian devil. *PLoS One*. 2017;12:e0168993.
56. Fritz FJ, Sengupta S, Harms RL, Tse DH, Poser BA, Roebroeck A. Ultra-high resolution and multi-shell diffusion MRI of intact ex vivo human brains using kT-dSTEAM at 9.4T. *Neuroimage*. 2019;202:116087.
57. Roebroeck A, Miller KL, Aggarwal M. Ex vivo diffusion MRI of the human brain: technical challenges and recent advances. *NMR Biomed*. 2019;32:e3941.
58. Leuze CWU, Anwander A, Bazin PL, et al. Layer-specific intracortical connectivity revealed with diffusion MRI. *Cereb Cortex*. 2014;24:328-339.
59. Kleinnijenhuis M, Zerbi V, Küsters B, Slump CH, Barth M, van Cappellen van Walsum AM. Layer-specific diffusion weighted imaging in human primary visual cortex in vitro. *Cortex*. 2013;49:2569-2582.
60. Adil SM, Calabrese E, Charalambous LT, et al. A high-resolution interactive atlas of the human brainstem using magnetic resonance imaging. *Neuroimage*. 2021;237:118135.
61. Lundell H, Nielsen JB, Ptito M, Dyrby TB. Distribution of collateral fibers in the monkey cervical spinal cord detected with diffusion-weighted magnetic resonance imaging. *Neuroimage*. 2011;56:923-929.
62. Ellingson BM, Kurpad SN, Schmit BD. Ex vivo diffusion tensor imaging and quantitative tractography of the rat spinal cord during long-term recovery from moderate spinal contusion. *J Magn Reson Imaging*. 2008;28:1068-1079.
63. Calabrese E, Adil SM, Cofer G, et al. Postmortem diffusion MRI of the entire human spinal cord at microscopic resolution. *NeuroImage Clin*. 2018;18:963-971.
64. Sosnovik DE, Wang R, Dai G, Reese TG, Wedeen VJ. Diffusion MR tractography of the heart. *J Cardiovasc Magn Reson*. 2009;11:47.
65. Angeli S, Befera N, Peyrat JM, Calabrese E, Johnson GA, Constantinides C. A high-resolution cardiovascular magnetic resonance diffusion tensor map from ex-vivo C57BL/6 murine hearts. *J Cardiovasc Magn Reson*. 2014;16:77.
66. Magat J, Yon M, Bihan-Poudec Y, Ozenne V. A group-wise registration and tractography framework for cardiac myofiber architecture description by diffusion MRI: an application to the ventricular junctions. *PLoS One*. 2022;17:e0271279.
67. Khalil C, Budzik JF, Kermarrec E, Balbi V, Le Thuc V, Cotten A. Tractography of peripheral nerves and skeletal muscles. *Eur J Radiol*. 2010;76:391-397.
68. Lehmann HC, Zhang J, Mori S, Sheikh KA. Diffusion tensor imaging to assess axonal regeneration in peripheral nerves. *Exp Neurol*. 2010;223:238-244.
69. Scharf A, Cheng TY, Urion R, Hostnik E. Ex vivo diffusion tensor imaging of the plantar nerves is feasible in the horse. *Am J Vet Res*. 2024;85:1-8.

15222594, 0, Downloaded from https://onlinelibrary.wiley.com/doi/10.1002/mrm.30424 by Ecole Polytech De Montreal, Wiley Online Library on [14/03/2025]. See the Terms and Conditions (https://onlinelibrary.wiley.com/terms-and-conditions) on Wiley Online Library for rules of use; OA articles are governed by the applicable Creative Commons License

70. Farinas AF, Manzanera Esteve IV, Pollins AC, et al. Diffusion tensor tractrography visualizes partial nerve laceration severity as early as 1 week after surgical repair in a rat model ex vivo. *Mil Med*. 2020;185:35-41.
71. Boyer RB, Kelm ND, Riley DC, et al. 4.7-T diffusion tensor imaging of acute traumatic peripheral nerve injury. *Neurosurg Focus*. 2015;39:E9.
72. Maharjan S, Chen J, Gaughan A, Chen NX, Wang N. Diffusion tractography of kidney by high angular resolution diffusion imaging. *Magn Reson Lett*. 2024;200117:200117.
73. Wang X, Cusick MF, Wang Y, et al. Diffusion basis spectrum imaging detects and distinguishes coexisting subclinical inflammation, demyelination and axonal injury in experimental autoimmune encephalomyelitis mice. *NMR Biomed*. 2014;27:843-852.
74. Khan AR, Cornea A, Leigland LA, Kohama SG, Jespersen SN, Kroenke CD. 3D structure tensor analysis of light microscopy data for validating diffusion MRI. *Neuroimage*. 2015;111:192-203.
75. Schilling KG, Janve V, Gao Y, Stepniewska I, Landman BA, Anderson AW. Histological validation of diffusion MRI fiber orientation distributions and dispersion. *Neuroimage*. 2018;165:200-221. doi:10.1016/j.neuroimage.2017.10.046
76. Budde MD, Janes L, Gold E, Turtzo LC, Frank JA. The contribution of gliosis to diffusion tensor anisotropy and tractography following traumatic brain injury: validation in the rat using Fourier analysis of stained tissue sections. *Brain*. 2011;134:2248-2260.
77. Grussu F, Bernatowicz K, Casanova-Salas I, et al. Diffusion MRI signal cumulants and hepatocyte microstructure at fixed diffusion time: insights from simulations, 9.4T imaging, and histology. *Magn Reson Med*. 2022;88:365-379.
78. Duval T, Saliani A, Nami H, et al. Axons morphometry in the human spinal cord. *Neuroimage*. 2019;185:119-128.
79. Bourne RM, Bailey C, Johnston EW, et al. Apparatus for histological validation of in vivo and ex vivo magnetic resonance imaging of the human prostate. *Front Oncol*. 2017;7:47.
80. Schilling K, Janve V, Gao Y, Stepniewska I, Landman BA, Anderson AW. Comparison of 3D orientation distribution functions measured with confocal microscopy and diffusion MRI. *Neuroimage*. 2016;129:185-197.
81. Morawski M, Kirilina E, Scherf N, et al. Developing 3D microscopy with CLARITY on human brain tissue: towards a tool for informing and validating MRI-based histology. *Neuroimage*. 2018;182:417-428.
82. Budde MD, Annese J. Quantification of anisotropy and fiber orientation in human brain histological sections. *Front Integr Neurosci*. 2013;7:3.
83. Kjer HM, Andersson M, He Y, et al. Bridging the 3D geometrical organisation of white matter pathways across anatomical length scales and species. 2024, doi:10.7554/elife.94917.2
84. Mollink J, van Baarsen KM, Dederen PJWC, et al. Dentatorubrothalamic tract localization with postmortem MR diffusion tractography compared to histological 3D reconstruction. *Brain Struct Funct*. 2016;221:3487-3501.
85. Eberle AL, Zeidler D. Multi-beam scanning electron microscopy for high-throughput imaging in connectomics research. *Front Neuroanat*. 2018;12:112.
86. Lee JY, Donato S, Mack AF, et al. Protocol for 3D virtual histology of unstained human brain tissue using synchrotron radiation phase-contrast microtomography. *Front Phys*. 2024;11-2023:11. doi:10.3389/fphy.2023.1335285
87. Foxley S, Sampathkumar V, De Andrade V, et al. Multi-modal imaging of a single mouse brain over five orders of magnitude of resolution. *Neuroimage*. 2021;238:118250.
88. Betz O, Wegst U, Weide D, et al. Imaging applications of synchrotron X-ray phase-contrast microtomography in biological morphology and biomaterials science. I. General aspects of the technique and its advantages in the analysis of millimetre-sized arthropod structure. *J Microsc*. 2007;227(1):51-71. Portico. doi:10.1111/j.1365-2818.2007.01785.x
89. Schaff F, Bech M, Zaslansky P, et al. Six-dimensional real and reciprocal space small-angle X-ray scattering tomography. *Nature*. 2015;527(7578):353-356. doi:10.1038/nature16060
90. Howard AF, Mollink J, Kleinnijenhuis M, et al. Joint modelling of diffusion MRI and microscopy. *Neuroimage*. 2019;201:116014.
91. Schilling K, Gao Y, Janve V, Stepniewska I, Landman BA, Anderson AW. Can increased spatial resolution solve the crossing fiber problem for diffusion MRI? *NMR Biomed*. 2017;30:e3787. doi:10.1002/nbm.3787
92. Mollink J, Kleinnijenhuis M, van Cappellen van Walsum AM, et al. Evaluating fibre orientation dispersion in white matter: comparison of diffusion MRI, histology and polarized light imaging. *Neuroimage*. 2017;157:561-574.
93. Budde MD, Frank JA. Examining brain microstructure using structure tensor analysis of histological sections. *Neuroimage*. 2012;63:1-10.
94. Alyami W, Kyme A, Bourne R. Histological validation of MRI: a review of challenges in registration of imaging and whole-mount histopathology. *J Magn Reson Imaging*. 2022;55:11-22.
95. Jespersen SN, Bjarkam CR, Nyengaard JR, et al. Neurite density from magnetic resonance diffusion measurements at ultrahigh field: comparison with light microscopy and electron microscopy. *Neuroimage*. 2010;49:205-216.
96. Leergaard TB, White NS, de Crespigny A, et al. Quantitative histological validation of diffusion MRI fiber orientation distributions in the rat brain. *PLoS One*. 2010;5:e8595.
97. Hansen B, Flint JJ, Heon-Lee C, et al. Diffusion tensor microscopy in human nervous tissue with quantitative correlation based on direct histological comparison. *Neuroimage*. 2011;57:1458-1465.
98. Baldi D, Aiello M, Duggento A, Salvatore M, Cavaliere C. MR imaging-histology correlation by tailored 3D-printed slicer in oncological assessment. *Contrast Media Mol Imaging*. 2019;2019:1071453.
99. Luciano NJ, Sati P, Nair G, et al. Utilizing 3D printing technology to merge MRI with histology: a protocol for brain sectioning. *J Vis Exp*. 2016;118:e54780. doi:10.3791/54780
100. Guy JR, Sati P, Leibovitch E, Jacobson S, Silva AC, Reich DS. Custom fit 3D-printed brain holders for comparison of histology with MRI in marmosets. *J Neurosci Methods*. 2016;257:55-63.
101. Mancini M, Casamitjana A, Peter L, et al. A multimodal computational pipeline for 3D histology of the human brain. *Sci Rep*. 2020;10:13839.

15222594, 0, Downloaded from https://onlinelibrary.wiley.com/doi/10.1002/mrm.30424 by Ecole Polytech De Montreal, Wiley Online Library on [14/03/2025]. See the Terms and Conditions (https://onlinelibrary.wiley.com/terms-and-conditions) on Wiley Online Library for rules of use; OA articles are governed by the applicable Creative Commons License

102. Annese J, Sforza DM, Dubach M, Bowden D, Toga AW. Post-mortem high-resolution 3-dimensional imaging of the primate brain: blockface imaging of perfusion stained tissue. *Neuroimage*. 2006;30:61-69.
103. Lebenberg J, Hérard AS, Dubois A, et al. Validation of MRI-based 3D digital atlas registration with histological and autoradiographic volumes: an anatomofunctional transgenic mouse brain imaging study. *Neuroimage*. 2010;51:1037-1046.
104. Huszar IN, Pallebage-Gamarallage M, Bangerter-Christensen S, et al. Tensor image registration library: deformable registration of stand-alone histology images to whole-brain post-mortem MRI data. *Neuroimage*. 2023;265:119792.
105. Choe AS, Gao Y, Li X, Compton KB, Stepniewska I, Anderson AW. Accuracy of image registration between MRI and light microscopy in the ex vivo brain. *Magn Reson Imaging*. 2011;29:683-692.
106. Howard AFD, Huszar IN, Smart A, et al. An open resource combining multi-contrast MRI and microscopy in the macaque brain. *Nat Commun*. 2023;14:4320.
107. Fox CH, Johnson FB, Whiting J, Roller PP. Formaldehyde fixation. *J Histochem Cytochem.* 1985; 33:845-853.
108. Breen MS, Lancaster TL, Wilson DL. Correcting spatial distortion in histological images. *Comput Med Imaging Graph.* 2005;29:405-417.
109. Pitiot A, Bardinet E, Thompson PM, Malandain G. Piecewise affine registration of biological images for volume reconstruction. *Med Image Anal.* 2006;10:465-483.
110. Dauguet J, Delzescaux T, Condé F, et al. Three-dimensional reconstruction of stained histological slices and 3D non-linear registration with in-vivo MRI for whole baboon brain. *J Neurosci Methods.* 2007;164:191-204.
111. Huszar IN, Pallebage-Gamarallage M, Bangerter-Christensen S, et al. Tensor image registration library: deformable registration of stand-alone histology images to whole-brain post-mortem MRI data. *Neuroimage.* 2023;265:119792.
112. Glover PM, Bowtell RW, Brown GD, Mansfield P. A microscope slide probe for high resolution imaging at 11.7 tesla. *Magn Reson Med*. 1994;31:423-428.
113. Flint JJ, Hansen B, Fey M, et al. Cellular-level diffusion tensor microscopy and fiber tracking in mammalian nervous tissue with direct histological correlation. *Neuroimage*. 2010;52:556-561.
114. Flint JJ, Hansen B, Portnoy S, et al. Magnetic resonance microscopy of human and porcine neurons and cellular processes. *Neuroimage*. 2012;60:1404-1411.
115. Flint JJ, Lee CH, Hansen B, et al. Magnetic resonance microscopy of mammalian neurons. *Neuroimage*. 2009;46:1037-1040.
116. Lee CH, Flint JJ, Hansen B, Blackband SJ. Investigation of the subcellular architecture of L7 neurons of Aplysia californica using magnetic resonance microscopy (MRM) at 7.8 microns. *Sci Rep*. 2015;5:11147.
117. Portnoy S, Flint JJ, Blackband SJ, Stanisz GJ. Oscillating and pulsed gradient diffusion magnetic resonance microscopy over an extended b-value range: implications for the characterization of tissue microstructure. *Magn Reson Med*. 2013;69:1131-1145.
118. Kor DZL, Jbabdi S, Huszar IN, et al. An automated pipeline for extracting histological stain area fraction for voxel-wise quantitative MRI-histology comparisons. *Neuroimage*. 2022;264:119726.
119. Bigun J, Bigun T, Nilsson K. Recognition by symmetry derivatives and the generalized structure tensor. *IEEE Trans Pattern Anal Mach Intell*. 2004;26:1590-1605.
120. Yendiki A, Aggarwal M, Axer M, Howard AFD, Anne-Marie van Cappellen van Walsum, Haber SN. Post mortem mapping of connectional anatomy for the validation of diffusion MRI. *Neuroimage* 2022;256(119146):119146.
121. Seehaus AK, Roebroeck A, Chiry O, et al. Histological validation of DW-MRI tractography in human postmortem tissue. *Cereb Cortex*. 2013;23:442-450.
122. Grisot G, Haber SN, Yendiki A. Diffusion MRI and anatomic tracing in the same brain reveal common failure modes of tractography. *Neuroimage*. 2021;239:118300.
123. Maffei C, Jovicich J, De Benedictis A, et al. Topography of the human acoustic radiation as revealed by ex vivo fibers micro-dissection and in vivo diffusion-based tractography. *Brain Struct Funct*. 2018;223:449-459.
124. Xu F, Shen Y, Ding L, et al. High-throughput mapping of a whole rhesus monkey brain at micrometer resolution. *Nat Biotechnol*. 2021;39:1521-1528.
125. Menzel M, Gräßel D, Rajkovic I, Zeineh MM, Georgiadis M. Using light and X-ray scattering to untangle complex neuronal orientations and validate diffusion MRI. *Elife*. 2023;12:e84024.
126. Abdollahzadeh A, Belevich I, Jokitalo E, Tohka J, Sierra A. Automated 3D axonal morphometry of White matter. *Sci Rep*. 2019;9:6084.
127. Livet J, Weissman TA, Kang H, et al. Transgenic strategies for combinatorial expression of fluorescent proteins in the nervous system. *Nature.* 2007;450:56-62.
128. Chung K, Wallace J, Kim SY, et al. Structural and molecular interrogation of intact biological systems. *Nature*. 2013;497:332-337.
129. Mai H, Rong Z, Zhao S, et al. Scalable tissue labeling and clearing of intact human organs. *Nat Protoc*. 2022;17:2188-2215.
130. Leuze C, Goubran M, Barakovic M, et al. Comparison of diffusion MRI and CLARITY fiber orientation estimates in both gray and white matter regions of human and primate brain. *Neuroimage*. 2021;228:117692.
131. Stolp HB, Ball G, So PW, et al. Voxel-wise comparisons of cellular microstructure and diffusion-MRI in mouse hippocampus using 3D bridging of optically-clear histology with neuroimaging data (3D-BOND). *Sci Rep*. 2018;8:4011.
132. Chang EH, Argyelan M, Aggarwal M, et al. The role of myelination in measures of white matter integrity: combination of diffusion tensor imaging and two-photon microscopy of CLARITY intact brains. *Neuroimage*. 2017;147:253-261.
133. Huang D, Swanson EA, Lin CP, et al. Optical coherence tomography. *Science*. 1991;254:1178-1181.
134. Menzel M, Reuter JA, Gräßel D, et al. Scattered light imaging: resolving the substructure of nerve fiber crossings in whole brain sections with micrometer resolution. *Neuroimage*. 2021;233:117952.
135. Axer M, Grässel D, Kleiner M, et al. High-resolution fiber tract reconstruction in the human brain by means of three-dimensional polarized light imaging. *Front Neuroinform*. 2011;5:34.

15222594, 0, Downloaded from https://onlinelibrary.wiley.com/doi/10.1002/mrm.30424 by Ecole Polytech De Montreal, Wiley Online Library on [14/03/2025]. See the Terms and Conditions (https://onlinelibrary.wiley.com/terms-and-conditions) on Wiley Online Library for rules of use; OA articles are governed by the applicable Creative Commons License

136. Wang H, Zhu J, Akkin T. Serial optical coherence scanner for large-scale brain imaging at microscopic resolution. *Neuroimage*. 2014;84:1007-1017.
137. Caspers S, Axer M, Caspers J, et al. Target sites for transcallosal fibers in human visual cortex - a combined diffusion and polarized light imaging study. *Cortex*. 2015;72:40-53.
138. Jones R, Maffei C, Augustinack J, et al. High-fidelity approximation of grid- and shell-based sampling schemes from undersampled DSI using compressed sensing: post mortem validation. *NeuroImage*. 2021; 244:118621. doi:10.1016/j.neuroimage.2021.118621
139. Jones R, Grisot G, Augustinack J, et al. Insight into the fundamental trade-offs of diffusion MRI from polarization-sensitive optical coherence tomography in ex vivo human brain. *Neuroimage*. 2020;214:116704.
140. Cloetens P, Barrett R, Baruchel J, Guigay J-P, Schlenker M. Phase objects in synchrotron radiation hard x-ray imaging. *J Phys D Appl Phys*. 1996;29(1):133–146. doi:10.1088/0022-3727/29/1/023
141. Walsh CL, Tafforeau P, Wagner WL, et al. Imaging intact human organs with local resolution of cellular structures using hierarchical phase-contrast tomography. *Nat Methods*. 2021;18(12):1532-1541. doi:10.1038/s41592-021-01317-x
142. Walsh CL, Tafforeau P, Wagner WL, et al. Imaging intact human organs with local resolution of cellular structures using hierarchical phase-contrast tomography. *Nat Methods*. 2021;18:1532-1541.
143. Fratzl P, Jakob HF, Rinnerthaler S, Roschger P, Klaushofer K. Position-Resolved Small-Angle X-ray Scattering of Complex Biological Materials. *J Appl Cryst*. 1997;30(5):765-769. doi:10.1107/s0021889897001775
144. Georgiadis M, Schroeter A, Gao Z, et al. Nanostructure-specific X-ray tomography reveals myelin levels, integrity and axon orientations in mouse and human nervous tissue. *Nat Commun*. 2021;12:2941.
145. Peddie CJ, Genoud C, Kreshuk A, et al. Volume electron microscopy. *Nat Rev Methods Primers*. 2022;2:51. doi:10.1038/s43586-022-00131-9
146. Yin W, Brittain D, Borseth J, et al. A petascale automated imaging pipeline for mapping neuronal circuits with high-throughput transmission electron microscopy. *Nat Commun*. 2020;11:4949.
147. Sepehrband F, Alexander DC, Kurniawan ND, Reutens DC, Yang Z. Towards higher sensitivity and stability of axon diameter estimation with diffusion-weighted MRI. *NMR Biomed*. 2016;29:293-308.
148. Assaf Y, Blumenfeld-Katzir T, Yovel Y, Basser PJ. AxCaliber: a method for measuring axon diameter distribution from diffusion MRI. *Magn Reson Med*. 2008; 59:1347-1354.
149. Barazany D, Basser PJ, Assaf Y. In vivo measurement of axon diameter distribution in the corpus callosum of rat brain. *Brain*. 2009;132:1210-1220.
150. West KL, Kelm ND, Carson RP, Alexander DC, Gochberg DF, Does MD. Experimental studies of g-ratio MRI in ex vivo mouse brain. *Neuroimage*. 2018;167:366-371.
151. Stikov N, Campbell JSW, Stroh T, et al. Quantitative analysis of the myelin g-ratio from electron microscopy images of the macaque corpus callosum. *Data Brief*. 2015;4:368-373.
152. Mohammadi S, Callaghan MF. Towards in vivo g-ratio mapping using MRI: unifying myelin and diffusion imaging. *J Neurosci Methods*. 2021;348:108990.
153. Ginsburger K, Matuschke F, Poupon F, Mangin JF, Axer M, Poupon C. MEDUSA: a GPU-based tool to create realistic phantoms of the brain microstructure using tiny spheres. *Neuroimage*. 2019;193:10-24.
154. Palombo M, Alexander DC, Zhang H. A generative model of realistic brain cells with application to numerical simulation of the diffusion-weighted MR signal. *Neuroimage*. 2019;188:391-402.
155. Callaghan R, Alexander DC, Zhang H, Palombo M. Contextual fibre growth to generate realistic axonal packing for diffusion MRI simulation. *Information Processing in Medical Imaging*. Springer International Publishing; 2019:429-440.
156. Winther S, Peulicke O, Andersson M, Kjer HM, Bærentzen JA, Dyrby TB. Exploring white matter dynamics and morphology through interactive numerical phantoms: the White Matter Generator. *Front Neuroinform*. 2024:18. doi:10.3389/fninf.2024.1354708
157. Andersson M, Kjer HM, Rafael-Patino J, et al. Axon morphology is modulated by the local environment and impacts the noninvasive investigation of its structure–function relationship. *PNAS*. 2020;117(52):33649-33659. doi:10.1073/pnas.2012533117
158. Knott G, Genoud C. Is EM dead? *J Cell Sci*. 2013;126:4545-4552.
159. Tsang TK, Bushong EA, Boassa D, et al. High-quality ultrastructural preservation using cryofixation for 3D electron microscopy of genetically labeled tissues. *Elife*. 2018;7. doi:10.7554/eLife.35524

How to cite this article: Schilling KG, Howard AFD, Grussu F, et al. Considerations and recommendations from the ISMRM Diffusion Study Group for preclinical diffusion MRI: Part 3—Ex vivo imaging: Data processing, comparisons with microscopy, and tractography. *Magn Reson Med*. 2025;1-22. doi: 10.1002/mrm.30424

15222594, 0, Downloaded from https://onlinelibrary.wiley.com/doi/10.1002/mrm.30424 by Ecole Polytech De Montreal, Wiley Online Library on [14/03/2025]. See the Terms and Conditions (https://onlinelibrary.wiley.com/terms-and-conditions) on Wiley Online Library for rules of use; OA articles are governed by the applicable Creative Commons License